

AN EXPLAINABLE PIPELINE FOR MACHINE LEARNING WITH FUNCTIONAL DATA

BY KATHERINE GOODE^{1,2,a}, J. DEREK TUCKER^{1,b}, DANIEL RIES^{1,c}, AND HEIKE HOFMANN^{2,d}

¹Statistical Sciences, Sandia National Laboratories, ^akjgoode@sandia.gov; ^bbjdtuck@sandia.gov; ^cdries@sandia.gov

²Department of Statistics, University of Nebraska–Lincoln, ^dhhofmann4@unl.edu

Machine learning (ML) models have shown success in applications with an objective of prediction, but the algorithmic complexity of some models makes them difficult to interpret. Methods have been proposed to provide insight into these "black-box" models, but there is little research that focuses on supervised ML when the model inputs are functional data. In this work, we consider two applications from high-consequence spaces with objectives of making predictions using functional data inputs. One application aims to classify material types to identify explosive materials given hyperspectral computed tomography scans of the materials. The other application considers the forensics science task of connecting an inkjet printed document to the source printer using color signatures extracted by Raman spectroscopy. An instinctive route to consider for analyzing these data is a data driven ML model for classification, but due to the high consequence nature of the applications, we argue it is important to appropriately account for the nature of the data in the analysis to not obscure or misrepresent patterns. As such, we propose the *Variable importance Explainable Elastic Shape Analysis (VEESA) pipeline* for training ML models with functional data that (1) accounts for the vertical and horizontal variability in the functional data and (2) provides an explanation in the original data space of how the model uses variability in the functional data for prediction. The pipeline makes use of elastic functional principal components analysis (efPCA) to generate uncorrelated model inputs and permutation feature importance (PFI) to identify the principal components important for prediction. The variability captured by the important principal components is visualized in the original data space. We ultimately discuss ideas for natural extensions of the VEESA pipeline and challenges for future research.

1. Introduction . Many machine learning models are considered “black-boxes” since their algorithmic complexity results in the inability to assign a physical meaning to the model parameters. In supervised learning, the interpretation of model parameters provides an understanding of the relationships between predictor and response variables. Understanding these relationships is beneficial for multiple reasons such as model assessment (e.g., is the model using variables in a scientifically reasonable manner?), data insight (e.g., what patterns in the data did the model find useful for prediction?), and helping to build trust in a prediction (e.g., do we feel comfortable making a decision based on how the model made use of the data to produce a prediction?). In lower consequence applications (e.g., movie recommendations or personalized advertisements), a lack of model “interpretability” may be permissible since incorrect predictions have minimal negative impacts, but in high-consequence areas such as national security and forensics science, it is difficult to motivate the use of a non-interpretable

Keywords and phrases: Elastic Shape Analysis, Explainability, Feature Selection, Functional Principal Components, Interpretability, Variable Importance.

model where model transparency is essential to avoid serious mistakes. Regardless of the consequence level of the application, interpretability provides information that helps gain data insight and improve models.

The desire to contextually explain how predictor variables relate to black-box predictions has led to a recent explosion of research focused on providing insight into black-box models (Adadi and Berrada, 2018; Guidotti et al., 2018; Zhang and Chen, 2020). This area of research is often referred to as explainable/interpretable machine learning (EML/IML) (Rudin, 2019)/(Molnar, Casalicchio and Bischl, 2020) or interpretable artificial intelligence (XAI) (Adadi and Berrada, 2018). While previous research considers various model and data types, there is minimal literature on EML for supervised learning with functional data inputs.

Each observation in a functional dataset consists of a collection of points representing a continuous curve or surface over a compact domain (e.g., a fixed length of time or region of space). Examples of functional data include the heights of children measured over time (Ramsay and Silverman, 2005) and silhouettes of animals extracted from images (Srivastava and Klassen, 2016). Modern technology has made the collection of functional data commonplace with devices such as glucose monitors (Danne et al., 2017), fitness trackers (Henriksen et al., 2018), and environmental sensors (Butts-Wilmsmeyer, Rapp and Guthrie, 2020). Functional data provide detailed information of a continuous process, but the form of the data requires special consideration to appropriately account for the functional structure.

One approach to analyzing functional data is to compute relevant summary statistics of the functions. This approach allows for the use of simpler statistical analyses but may result in loss of information and incorrect inference (Tucker, Wu and Srivastava, 2013; Srivastava and Klassen, 2016). Instead, methods have been developed that treat the underlying curve as an infinite dimensional continuous function such as functional regression, functional ANOVA, and functional principal component analysis (fPCA) (Ramsay and Silverman, 2005).

In machine learning, functional data are used as inputs to predict an outcome based on the functional shapes (e.g., Li et al. (2014), Zhang (2019), and Ries and Gabriel Huerta (2023)). Various modeling approaches have been suggested (e.g., Rossi et al. (2005), Tian (2010), and Barinder Thind and Cao (2023)). One approach is to create vectors of values across functions at each domain location (e.g., time or location) and use these “*cross-sectional*” vectors as model input features (Tian, 2010). A clear downside to the cross-sectional approach is that the dependence between observations within a function is ignored. Another approach is to apply a dimension reduction technique, such as fPCA, and use a subset of the transformed features as predictor variables (Rossi et al., 2005; Tian, 2010).

A few papers consider explainability with functional data inputs. Martin-Barragan, Lillo and Romo (2014) and Barinder Thind and Cao (2023) adapt the methodology of support vector machines and neural networks, respectively, to account for functional data. The models are constructed so the parameters can be visualized and interpreted in the context of the functional data domain. Goode, Ries and Zollweg (2020) use fPCA for dimension reduction and feature importance to identify important functional principal components (fPCs).

All previously proposed methods for using functional data as inputs to machine learning models only account for *vertical* functional variability, where vertical variability (also known as y or amplitude variability) is the variability in the height of functions. Tucker, Wu and Srivastava (2013) highlights that functional data possess both vertical and *horizontal* variability. Horizontal variability (also known as x or phase variability) is the variability in the location of peaks and valleys of the functions. (See Tucker, Wu and Srivastava (2013) for mathematical definitions.) If one variability is ignored, the resulting functional data analysis may not accurately capture the structure in the data.

In this paper, we consider two classification tasks with functional data from high consequence decision spaces. The first application aims to identify explosive materials given

hyperspectral computed tomography scans of the material for national security purposes. The second application is motivated by illicit uses of inkjet printers, such as the creation of counterfeit currency. Forensic investigators are interested in being able to identify the source printer for a printer document based on Raman spectroscopy signatures extracted from the document. We propose a novel explainable machine learning pipeline for functional data inputs to analyze these data. The approach, which we refer to as the *Variable importance Explainable Elastic Shape Analysis (VEESA) pipeline*, (1) accounts for the vertical and horizontal variability in the functional data and (2) provides an explanation in the original data space of how the model uses variability in the functional data for prediction.

The pipeline uses a principal component analysis for functional data derived using the elastic shape analysis (ESA) framework (Joshi et al., 2007; Srivastava et al., 2011; Tucker, Wu and Srivastava, 2013) referred to as *elastic fPCA (efPCA)*. Similar to the use of fPCA with machine learning, the observed functions are converted to fPCs and used as predictor variables, but unlike fPCA, efPCA accounts for vertical and horizontal functional variability. Elastic functional principal components (efPCs) have been used previously in modeling approaches (Tucker, Lewis and Srivastava, 2019; Tucker et al., 2020), but there no literature on the use of efPCA with explainability for machine learning. After the model is trained, the model agnostic method of permutation feature importance (PFI) (Fisher, Rudin and Dominici, 2019) is applied to identify important efPCs. PFI is known to be biased when correlation is present between variables (Hooker, Mentch and Zhou, 2021), but since principal components (PCs) are uncorrelated, there is no concern of feature importance bias due to correlation in the VEESA pipeline. Visualization is used to interpret the important efPCs. The visualizations depict the variability captured by the important efPCs in the original data space, which allows both model developers and subject matter experts to determine whether the model is drawing on reasonable phenomenological characteristics for prediction.

This paper is structured as follows. In Section 2, background is provided on the methods of efPCA and PFI. Section 3 describes the VEESA pipeline in detail. Section 4 presents the VEESA pipeline analyses of the explosive material and inkjet printer applications. We discuss the advantages and limitations of the VEESA pipeline and possible future research directions in Section 5.

2. Background . In this section, we provide background on the separation of vertical and horizontal functional variability (Section 2.1), efPCA (Section 2.2), and PFI (Section 2.3). We introduce a simulated dataset based on an example from Tucker, Wu and Srivastava (2013) to demonstrate these methods. We will refer to this data as the *shifted peaks* data. The shifted peaks data are available from the *veesa* R package (Goode and Tucker, 2024), and the code associated with all analyses of the shifted peaks data in this paper is available at github.com/sandialabs/veesa/tree/master/demos/goode-et-al-paper.

The shifted peaks data contain 500 functions from two groups with 250 functions per group (Figure 1 (top left)). The functions are simulated as

$$(1) \quad y_{g,i}(t) = z_{g,i} e^{-(t-a_{g,i})^2/2}$$

where $g = 1, 2$ indicates the group, $i = 1, 2, \dots, 250$ identifies a function within a group, $t \in [-15, 15]$, $z_{g,i} \stackrel{iid}{\sim} N(\mu_{z,g}, (0.05)^2)$, and $a_{g,i} \stackrel{iid}{\sim} N(\mu_{a,g}, (1.25)^2)$. We set $\mu_{z,1} = 1$, $\mu_{z,2} = 1.25$, $\mu_{a,1} = -3$, and $\mu_{a,2} = 3$, so the true functional mean of group 1 has a peak that is lower and further to the left than group 2 (solid lines in Figure 1 (top right)). The functions are generated with 150 equally spaced observations per function. For prediction, the functions are randomly separated into training and testing sets with 400 and 100 functions, respectively.

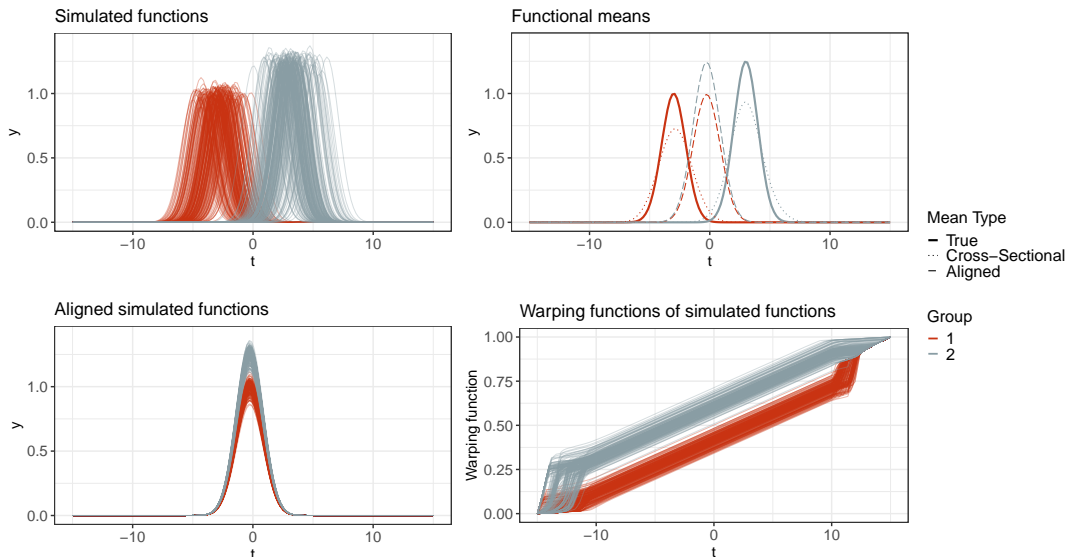


FIG 1. (Top Left) Training data functions from the shifted peak simulated data. (Top Right) The true, cross-sectional, and aligned functional means. (Bottom Left) The aligned functions. (Bottom Right) The warping functions from the alignment of the functions.

2.1. *Separation of Vertical and Horizontal Variability*. As previously mentioned, there are two types of variability present in functional data: vertical and horizontal variability. The shifted peaks data in Figure 1 (top left) exemplify vertical variability by the differences in peak intensity and horizontal variability by the difference in peak times. The dotted lines in Figure 1 (top right) demonstrate an example of how ignoring horizontal variability can lead to inaccurate representations of the functional forms. The dotted lines represent the cross-sectional group means of the shifted peaks data (i.e., mean value computed across all functions at a time). Both cross-sectional means have different shapes than the true means, which are narrower and have higher peaks than the cross-sectional means.

Tucker, Wu and Srivastava (2013) account for both variabilities in eFPCA by first decomposing observed functions into two new sets of functions: aligned and warping functions. Aligned functions match the peaks and valleys from the observed functions, and thus, capture the vertical variability present in the observed functions. Warping functions transform the observed functions to the aligned functions, and thus, capture the horizontal variability in the observed functions. The separation process described in Tucker, Wu and Srivastava (2013) uses methodology from the ESA framework described in Srivastava et al. (2011) and Joshi et al. (2007). Here, we provide an overview of the separation process and refer the reader to those papers and Srivastava and Klassen (2016) for more information.

We start by letting f be a real-valued function with the domain $[0, 1]$; this domain can be easily generalized to any other compact subinterval of \mathbb{R}^1 . We assume that all functions considered in the following analysis are observed on the same interval. Furthermore, for concreteness, only functions that are absolutely continuous on $[0, 1]$ will be considered, and we let \mathcal{F} denote the set of all such functions. In practice, the observed data are discrete, so this assumption is not a restriction. Also, let Γ be the set of orientation-preserving diffeomorphisms of the unit interval $[0, 1]$:

$$\Gamma = \{\gamma : [0, 1] \rightarrow [0, 1] \mid \gamma(0) = 0, \gamma(1) = 1, \gamma \text{ is a diffeomorphism}\}.$$

Elements of Γ play the role of warping functions. For any $f \in \mathcal{F}$ and $\gamma \in \Gamma$, the composition $f \circ \gamma$ denotes the time warping of f by γ (i.e., the aligned version of f).

As described in [Tucker, Wu and Srivastava \(2013\)](#), there are two metrics to measure the amplitude and phase variability of functions. These metrics are proper distances, one on the quotient space \mathcal{F}/Γ (i.e., amplitude) and the other on the group Γ (i.e., phase). The amplitude or y -distance for any two functions $f_1, f_2 \in \mathcal{F}$ is defined as

$$(2) \quad d_a(f_1, f_2) = \inf_{\gamma \in \Gamma} \|q_1 - (q_2 \circ \gamma)\sqrt{\dot{\gamma}}\|,$$

where $q(t) = \text{sign}(\dot{f}(t))\sqrt{|\dot{f}(t)|}$ is known as the *square-root velocity function (SRVF)* (\dot{f} is the time derivative of f). The SRVF transformation of f is used in the distance computation since if f is absolutely continuous, q is square-integrable, which allows $d_a(f_1, f_2)$ to be a proper distance. This is unlike other functional alignment processes (of the type $\inf_{\gamma \in \Gamma} \|f_1 - f_2 \circ \gamma\|$) that are not proper distances. For more details on the SRVF transformation, see [Srivastava et al. \(2011\)](#). The distance in Equation 2 is solved using the dynamic programming algorithm ([Bertsekas, 1996](#)).

The second metric is the phase or x -distance for measuring the distance between two warping functions $\gamma_1, \gamma_2 \in \Gamma$. Since Γ is an infinite-dimensional nonlinear manifold (i.e., not a standard Hilbert space), it is challenging to compute a distance on Γ . A transformation is applied to the warping functions to simplify the complicated geometry of Γ . Specifically, the SRVF of γ is computed: $\psi = \sqrt{\dot{\gamma}}$. Note that $\dot{\gamma} > 0$. Let Ψ be the set of all such ψ 's, which can be shown to be the Hilbert sphere (i.e., $\Psi = \mathbb{S}_\infty^+$, the positive orthant of the Hilbert sphere). For two warping functions $\gamma_1, \gamma_2 \in \Gamma$, the x -distance is computed as

$$(3) \quad d_p(\gamma_1, \gamma_2) = d_\psi(\psi_1, \psi_2) = \cos^{-1} \left(\int_0^1 \psi_1(t)\psi_2(t)dt \right),$$

the arc-length between the SRVFs of the warping functions on the Hilbert sphere. Note that ψ is invertible, which makes it possible to reconstruct γ from ψ as $\gamma(t) = \int_0^t \psi(s)^2 ds$ since $\gamma(0) = 0$.

For separating the phase-amplitude components of a set of functions f_1, f_2, \dots, f_n , we first compute a Karcher mean of the given functions (denoted by $\mu_f \in \mathcal{F}$ and μ_q in SRVF space) under the metric d_a :

$$(4) \quad (\text{In } \mathcal{F} \text{ space}) : \mu_f = \arg \min_{f \in \mathcal{F}} \sum_{i=1}^n d_a(f, f_i)^2$$

$$(5) \quad (\text{In SRVF space}) : \mu_q = \arg \min_{q \in \mathbb{L}^2} \sum_{i=1}^n \left(\inf_{\gamma_i \in \Gamma} \|q - (q_i, \gamma_i)\|^2 \right),$$

where $(q_i, \gamma_i) = (q_i \circ \gamma_i)\sqrt{\dot{\gamma}_i}$. Note that these formulations are equivalent. That is, $\mu_q = \text{sign}(\dot{\mu}_f)\sqrt{|\dot{\mu}_f|}$. As described in [Srivastava et al. \(2011\)](#), the algorithm for computing the Karcher mean also results in (1) aligned functions $\{\tilde{f}_1, \tilde{f}_2, \dots, \tilde{f}_n\}$ where $\tilde{f}_i = f_i \circ \gamma_i$, representing the amplitude variability and (2) the warping functions $\{\gamma_1, \gamma_2, \dots, \gamma_n\}$ used in aligning the original data and representing the phase variability.

We apply the separation method to the shifted peaks data. Figure 1 (bottom left and bottom right) shows the aligned and warping functions, respectively. The dashed lines in Figure 1 (top right) are the cross-sectional group means from the aligned functions. With the horizontal variability removed, the group means of the aligned functions correctly capture the shape of the true group means (ignoring peak timing).

2.2. *Elastic Functional Principal Component Analysis*. There are three efPCA methods that model functional variability: *vertical*, *horizontal*, and *joint fPCA* (vfPCA, hfPCA, and jfPCA). vfPCA and hfPCA are proposed in Tucker, Wu and Srivastava (2013). As their names suggest, vfPCA and hfPCA provide separate evaluations of the horizontal and vertical variabilities present in the functions using the aligned and warping functions, respectively. Lee (2017) proposed jfPCA (or combined fPCA), which jointly accounts for vertical and horizontal variability by concatenating the warping and aligned functions into a combined function, g^C , before computing principal components. Tucker et al. (2020) make a modification to the methodology proposed by Lee (2017) by constructing the combined function g^C using the SRVF \tilde{q} of the aligned function \tilde{f} , since \tilde{q} is guaranteed to be an element of \mathbb{L}^2 . We use the modified version by Tucker et al. (2020) in this paper. We provide a generalized version of the process for computing efPCs here, and we refer the reader to (Tucker, Wu and Srivastava, 2013), (Lee, 2017), and (Tucker et al., 2020) for further details.

TABLE 1
Functional Principal Component Domains.

	Vertical fPCA	Horizontal fPCA	Joint fPCA
Representation	\tilde{q}	γ	$g^C = [\tilde{q} \ C v(t)]$
Variability	Amplitude	Phase	Amplitude + Phase
Metric	Fisher-Rao	Fisher-Rao	Fisher-Rao

For a set of functions $\{f_1, f_2, \dots, f_n\}$, separate the functions into aligned $\{\tilde{f}_1, \tilde{f}_2, \dots, \tilde{f}_n\}$ and warping $\{\gamma_1, \gamma_2, \dots, \gamma_n\}$ functions using the method described in Section 2.1. Next, compute a sample covariance function on the functional representation shown in Table 1 based on the variability of interest. For joint fPCA, C is a constant such that $C > 0$, and $v(t)$ is a tangent space representation of $\psi(t)$, which is used for computational ease. See (Lee, 2017) for a data-driven approach for estimating C and Tucker et al. (2020) for details on the computation of $v(t)$. For a generalization, let z_1, z_2, \dots, z_n represent the set of functions capturing the specified type of variability (i.e., \tilde{q} , γ , or $g^C = [\tilde{q} \ C v(t)]$). The sample covariance function is computed as

$$(6) \quad K = \frac{1}{n-1} \sum_{i=1}^n (z_i - \hat{\mu}_z)(z_i - \hat{\mu}_z)^T.$$

where $\hat{\mu}_z$ is the sample mean function. Next, apply singular value decomposition (SVD) to the covariance matrix to obtain $K = U_K \Sigma_K V_K^T$ where U_K contains the directions of principal variability. The principal coefficients are computed as $\langle z_i, U_{K,j} \rangle$.

The principal directions can be visualized in the original function space, \mathcal{F} , to interpret functional variability captured by fPCs. A common visualization is to plot the Karcher mean and the variation in the principal directions. In an abuse of notation, we represent a generalized form of this as

$$(7) \quad \mu_z \pm \sqrt{\tau \Sigma_{K,jj}} U_{K,j}$$

where $\tau \in \mathbb{N}^+$. By plotting a series of curves given various values of τ , the visualization provides a visual spectrum of the variability of shapes of functions captured by the principal component. We refer to these as plots of the *principal direction plots*.

Figure 2 shows the principal direction plots for the first joint functional principal component (jfPC) from an application of jfPCA to the shifted peaks data. The application of jfPCA

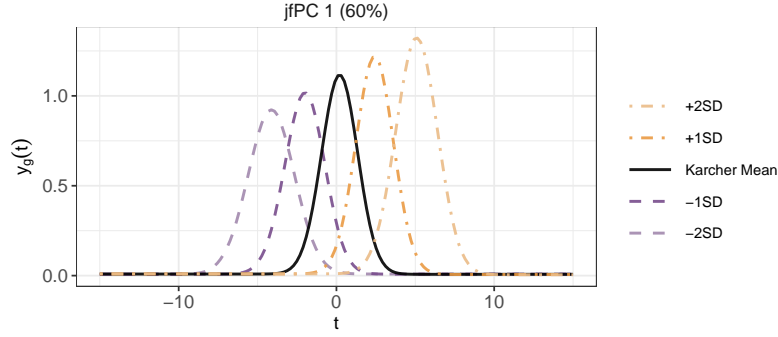


FIG 2. Plot of the principal directions for interpreting the functional variability captured by jfPC 1 from the shifted peaks data shown in Figure 1.

is done using the *fdasrsf* R package (Tucker, 2024a). The solid black line represents the Karcher functional mean. The dashed/dashed-dotted lines represent the principal directions plus/minus 1 and 2 standard deviations. The visual indicates that the first principal component captures a large amount of variability in peak time and variability in peak intensity, which agrees with the functional variability seen in Figure 1 (top left).

2.3. Permutation Feature Importance . Permutation feature importance (PFI) was initially developed as a tool for random forests by Breiman (2001). Fisher, Rudin and Dominici (2019) recognized that the process could be generalized to any model type, which allows for comparison of feature importance across model types. The objective of PFI is to quantify the importance of a predictor variable by measuring the change in model performance on a set of data when the predictor variable is randomly permuted. The variable is considered important if the model performance worsens considerably when the variable is permuted in comparison to the model predictions on the observed data.

There is some variability in how PFI has been previously defined. In this paper, we define PFI using the following definition. Let \mathcal{A} be a model, \mathbf{X} be an $n \times p$ data matrix with n observations and p predictor variables, X_1, X_2, \dots , and X_p be the columns of \mathbf{X} , and m be a performance metric computed on \mathbf{X} with model \mathcal{A} . The data \mathbf{X} may be training data, testing data, or another set of data of interest. PFI provides insight into how the model \mathcal{A} makes use of the data to provide predictions. The results may differ between the training and testing data. The performance metric m may be any metric of interest such that larger values indicate better performance. Examples include negative mean squared error for regression and accuracy for classification.

Define PFI for variable $j \in \{1, \dots, p\}$ as follows. For repetition $r \in \{1, \dots, R\}$:

1. Randomly permute X_j . Define the permuted variable as $\tilde{X}_{j,r}$.
2. Create a new dataset, $\tilde{\mathbf{X}}_{j,r}$, by replacing X_j in \mathbf{X} with $\tilde{X}_{j,r}$.
3. Compute $m_{j,r}$ as the performance metric on $\tilde{\mathbf{X}}_{j,r}$ for model \mathcal{A} .
4. Then, the PFI for variable j is equal to

$$\mathcal{I}_j = m - \frac{1}{R} \sum_{r=1}^R m_{j,r}.$$

\mathcal{I}_j is interpreted as the average change in model performance when j is randomly permuted. For example, if accuracy is used for m , PFI is interpreted as, “on average, the accuracy of model \mathcal{A} decreased by \mathcal{I}_j when feature j is randomly permuted”. An example of PFI computed on the shifted peaks data is included in Section 3.

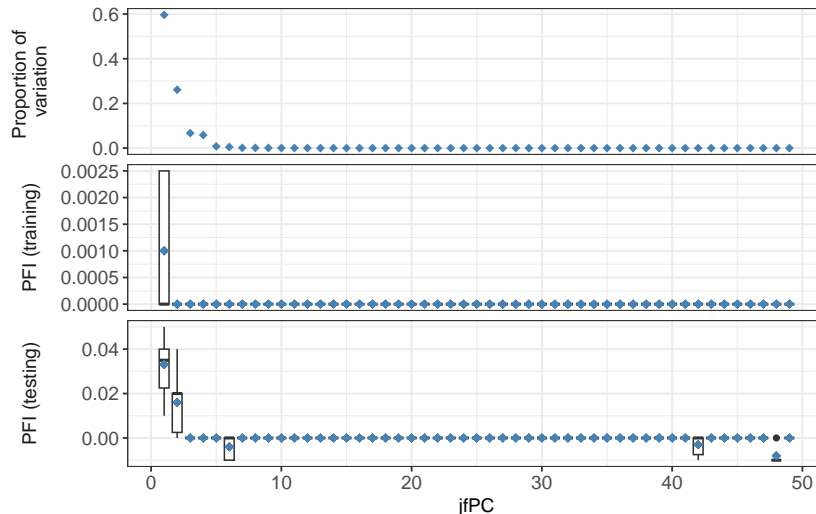


FIG 3. (Top) Proportion of variation explained by the jfPCs computed from the shifted peaks data. (Middle) Boxplots of PFI values across replicates associated with each jfPC from the shifted peaks data random forest computed on the training data. The blue diamonds represent the PFI value averaged over replicates. (Bottom) Same as middle plot but computed on the shifted peaks test data.

In addition to considering the quantity of \mathcal{I}_j , it may be valuable to consider the variability of the change in model performance across repetitions. Thus, define the feature importance for variable j and a single repetition r as $\mathcal{I}_{j,r} = \mathbf{m} - \mathbf{m}_{j,r}$. We may compute the standard deviation and create visualizations capturing the variability in $\mathcal{I}_{j,r}$ across the R repetitions. A large variation in $\mathcal{I}_{j,r} = \mathbf{m} - \mathbf{m}_{j,r}$ indicates that the change in model performance is dependent on the permutation of variable j , and more replications may be needed to obtain a good estimate of the average PFI.

3. Methods . In this section, we present the VEESA pipeline. As previously stated, the VEESA pipeline is a procedure for training and explaining machine learning models in applications where functional data are used to predict an outcome. By making use of the ESA framework, the VEESA pipeline mathematically captures the continuous nature of the observed functions and accounts for the vertical and horizontal variability that may be present in the functions. We first describe the application of the VEESA pipeline to training data for model building in Section 3.1. We then describe how the pipeline is applied to test/validation data in Section 3.2. Lastly, in Section 3.3, we describe the intended uses for the VEESA pipeline explanations. A comparison of the results to the cross-sectional approach is included in the supplemental material. The methodology described here is implemented in the *veesa* R package (Goode and Tucker, 2024) and Python functions provided at github.com/sandialabs/veesa/tree/master/demos/goode-et-al-paper. The R and Python code use the *fdasrf* R package (Tucker, 2024a) and the *fdasrvf* (Tucker, 2024b) packages, respectively, to apply functional alignment and efPCA.

3.1. *VEESA Pipeline (Training Data)* . In order to obtain an accurate estimate of model predictive performance on new data, supervised machine learning models are typically fit to a set of training data and then used to obtain predictions on a set of held out data (i.e., either testing or validation data). We begin by describing the steps in the VEESA pipeline as applied to training data. We include an example of each step applied to the shifted peaks data from Section 2 except for the smoothing step since the data are simulated as smooth functions.

3.1.1. *Step 1: Smoothing.* If the observed functions are not smooth, begin by applying a smoothing technique to the individual functions in the training data such as a box filter (Tucker, Wu and Srivastava, 2013) or splines (Ullah and Finch, 2013). The SRVF transformation in the separation of vertical and horizontal variability requires the computation of a derivative. As a result, it is recommended that smoothing is applied to observed functions before the variability separation process to compute an accurate estimate of the derivative, and in turn, the SRVF. The choice of the smoothing method is left to the analysts. In order to determine how much to smooth the functions, we suggest treating the amount of smoothing as a tuning parameter in the VEESA pipeline and conducting a cross-validation analysis to identify the amount of smoothing that results in the best predictive performance.

3.1.2. *Step 2: Separation of Functional Variability.* Apply the ESA alignment process described in Section 2.1 to the training data. As previously described, the aligned and warping functions from the shifted peaks training data are shown in Figure 1.

3.1.3. *Step 3: Elastic Functional Principal Component Analysis.* Apply one of the efPCA methods described in Section 2.2 to the training data. The selection of a method will depend on the relationship between the functional form and the response variable. If predictive information is only contained in the vertical or horizontal direction, then vfPCA or hfPCA, respectively, would be applicable. However, if predictive information is contained in both types of variability, then jfPCA should be used. If it is not known whether predictive information is associated with vertical variability, horizontal variability, or both, all methods could be applied to determine which leads to the best predictive performance. Figure 3 (top) shows the proportion of variance explained by jfPCs computed on the shifted peaks training data. Since we know predictive information is contained in both vertical and horizontal variability in the shifted peaks data, we use jfPCA.

3.1.4. *Step 4: Model Training.* Train a model using the efPCs obtained in Step 3 as predictor variables. Since the amount of variability explained by a principal component does not indicate the predictive ability of a principal component, we recommend initially training a model with all (or a large number of) efPCs. Feature selection may be performed after obtaining PFI results. For the shifted peaks data, a random forest is trained using the *randomForest* package in R (Liaw and Wiener, 2002) with the default settings. The jfPCs obtained in Step 3 are used as the predictor variables, and the group as the response variable. The model returns an accuracy of 1 on training data. The test data accuracy is provided in Section 3.2.

3.1.5. *Step 5: Permutation Feature Importance.* Apply PFI, as described in Section 2.3, to determine the importance of the efPCs. Since efPCs are orthogonal, there is no concern of bias in the results due to correlation between predictor variables. The use of PFI as the explainability method provides two key advantages. First, PFI is model agnostic, so variable importance is comparable across model types and can potentially assist with model selection. Second, PFI is relatively simple to understand, which makes it possible to explain to decision makers who may have little familiarity with machine learning models. However, other explainability methods could easily be substituted such as partial dependence plots (Friedman, 2001). The PFI values for the random forest trained on the shifted peaks data are computed on the training data using a metric of accuracy and 10 replications. Figure 3 (middle) shows the PFI results for the random forest from Step 4. The boxplots depict the PFI values across replicates, and the diamonds indicate the PFI value averaged over replicates. jfPC 1 is clearly the most important predictor variable in the random forest (with some replicates returning a change in accuracy of 0). The value of PFI (averaged across replicates) for jfPC 1 is interpreted as follows: on average, the random forest accuracy (on the training data) decreases by

0.001 when jfPC 1 is randomly permuted. The variability across replicates for jfPC 1 and the relatively small change in accuracy provides some evidence that while the PFI values are 0 for all other jfPCs, the model is drawing on information from at least one of the other jfPCs.

3.1.6. *Step 6: efPC Visualizations.* PFI identifies the efPCs important to the model, but visualizations are needed to interpret the functional variability used by the model for prediction. Specifically, the efPCs are interpreted using principal direction plots as discussed in Section 2.2. The principal direction plots depict the functional variability captured by a principal component on the original data space. This representation is advantageous to subject matter experts who are used to working with functions on this space and likely have an intuition as to the functional variability that would be expected to be related to a distinction between classes. The principal direction plot for jfPC 1 from the shifted peak data (Figure 2) indicates that jfPC 1 captures variability in both peak time and intensity based on the known distinction between the functional group means.

3.2. *VEESA Pipeline (Testing Data).* After the application of the VEESA pipeline to the training data, the pipeline steps may be applied to additional data such as test data. The general process remains the same but with some implementation adjustments for certain steps.

1. *Smoothing* Apply the same smoothing process as is applied to the training data.
2. *Separation of Functional Variability* The alignment of test data is implemented by aligning the test data functions to the Karcher Mean of the training data SRVFs. That is, for a set of training data functions $\{f_1, f_2, \dots, f_n\}$ and a set of test data functions $\{f_{n+1}, f_{n+2}, \dots, f_{n+m}\}$, compute SRVFs of the test data functions $\{q_{n+1}, q_{n+2}, \dots, q_{n+m}\}$. Let $\hat{\mu}_q$ represent the sample Karcher mean of the training data functions in SRVF space. Compute the warping functions $\{\gamma_{n+1}, \gamma_{n+2}, \dots, \gamma_{n+m}\}$ that align the test data SRVFs to $\hat{\mu}_q$. That is,

$$(8) \quad \gamma_{n+j} = \arg \min_{\gamma \in \Gamma} \|\hat{\mu}_q - (q_{n+j} \circ \gamma) \sqrt{\hat{\gamma}}\|,$$

where $j = 1, \dots, m$. The warping functions computed on the test data, γ_{n+j} , are then used to compute the aligned test data functions: $(q_{n+j} \circ \gamma) \sqrt{\hat{\gamma}_{n+j}}$ (in SRVF space).

3. *Elastic Functional Principal Component Analysis* As described in Section 2.2, the specifics of computing efPCs on the test data will vary based on the efPCA method applied to the training data, but the general concept is the same. Let $z_{n+1}, z_{n+2}, \dots, z_{n+m}$ represent the set of functions computed in the alignment process of the test data associated with the desired efPCA method. Then the principal coefficients are computed as $\langle z_{n+j}, U_{K,j} \rangle$ for $j = 1, \dots, m$, where $U_{K,j}$ contains the directions of principal variability computed when efPCA is applied to the training data. Note that this multiplication is done on the SRVF space and can then be converted back to the original space.
4. *Model* The efPCs computed on the test data are input into the previously trained model to obtain predictions.
5. *Permutation Feature Importance* PFI is computed on the test data. The efPCs that are important for the test data may be different than those that are important for the training data. If there is a difference, it may suggest that test data contains observations that are out of distribution compared to the training data.
6. *Visualization of efPCs* Create visualizations of the principal directions for any important efPCs not previously considered.

We apply the above steps to the shifted peaks test data functions using the random forest model described in Section 3.1. The test data accuracy is 0.99. The resulting PFI values on

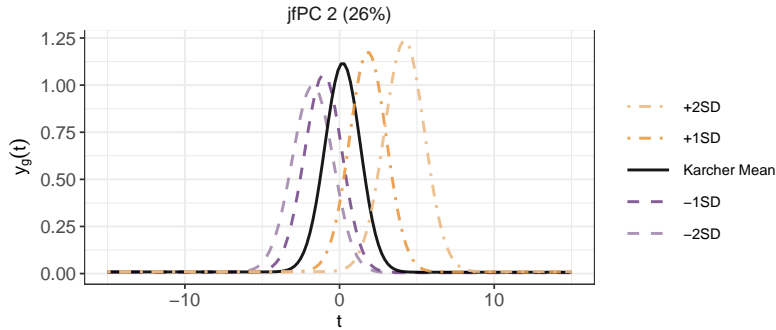


FIG 4. Plot of the principal directions for interpreting the functional variability captured by jfPC 2 from the shifted peaks data shown in Figure 1.

the test data are depicted in Figure 3 (bottom). Note that the magnitude of the importance is larger for the test data than the training data (i.e., a PFI value of 0.033 for jfPC 1 on the test data compared to a PFI value of 0.001 for jfPC 1 on the training data). It would be interesting to explore this further to better understand the reasons for the magnitude difference. In the training data, only jfPC 1 has importance, but with the test data, both jfPC 1 and 2 show importance. There are also several PCs with negative PFI values on the test data, which suggests that the model performs better with these variables removed.

Recall that Figure 2 shows the principal directions associated with jfPC 1, which indicated that jfPC 1 captures joint variability in peak time and peak intensity. Figure 4 shows the principal directions associated with jfPC 2. jfPC 2 appears to capture both horizontal and vertical variable between functions that is more nuanced than jfPC 1: functions that are similar to the Karcher mean and functions that are different. Both of these aspects of the variability in the shifted peaks functions makes sense to be useful for classifying the two groups.

3.3. Intended Use . The development of explanations for machine learning models is dictated by the intended audience. For example, an explanation intended for a model developer who is knowledgeable about the technical details of a model may be more technical. However, an explanation intended to promote the use of a model to a decision maker (e.g., a medical doctor or courtroom jury member) will likely need to take a less technical form for an individual who is not familiar with the technical details of the model. In this section, we clarify that the intended use for the explanations from the VEESA pipeline are intended to be used by analysts for model development. Additional work is needed to determine useful approaches for distilling the information gained from the VEESA pipeline to decision makers who are not knowledgeable about the technical details of machine learning models. However, anecdotal experience has shown us that the resulting explanations from the VEESA pipeline can also be useful to the application subject matter experts since the explanations are presented in the data space that the experts are used to working with. This allows the subject matter experts to connect the functional variability identified as important to their scientific understanding of the underlying mechanism.

The intended uses for the explanations produced by the VEESA pipeline are:

- **Variable Selection:** At this point in the model development process, an analyst can use the PFI results to help with variable selection. PFI determines the efPCs that are globally important to a model for prediction. Thus, a new model can be trained using a reduced number of efPCs selected based on PFI. The efPCs with low variable importance will likely capture variability created by noise in the data or factors unrelated to the response variable. The removal of these efPCs from a model may improve predictive performance.

- *Model Comparison*: If multiple models are trained (including different model types), the VEESA pipeline helps analysts determine if the models are using similar or different characteristics of the functional variability. If the characteristics are different, the information may help in selection of a model. For example, a model that uses the most reasonable variables based on the scientific understanding of the application may be more desirable since the predictions can be explained. Another scenario is that a model that has fewer important principal components with comparable predictive performance may be more desirable for easier interpretability.
- *Gaining Model Trust*: Model trust is built through many aspects (e.g., predictive performance, code accuracy, etc.), and one such aspect is whether the data are being utilized by the model in a scientifically reasonable manner. The VEESA pipeline allows analysts to identify the aspects of functions that are used by a model for discrimination and determine if the functional variability important to the model is reasonable based on an understanding of the phenomenology of the data. Trust is gained in the model if reasonable data characteristics are used for discrimination. For example, the PFI results from the shifted peaks data indicate that the random forest is using peak height and timing to classify function to a group. Since we know that this is the main phenomenological characteristic that distinguishes the two classes, we gain trust in the model. If the PFI results indicated that only jFPCs that captured vertical variability were important, we would have been suspicious of the model not accurately capturing the appropriate information in the data. Of course, we know the true generating mechanism for the shifted peaks data, which will not be the case with real data. However, subject matter expert knowledge could be used to inform whether the model is considering reasonable data characteristics and/or missing data characteristics that should be informative.

4. Examples . In this section, we present two examples that utilize the VEESA pipeline to train machine learning models with functional data inputs and gain insight into the models. Section 4.1 applies a neural network to identify an explosive from a set of materials using hyperspectral computed tomography (H-CT) scans. Section 4.2 applies a random forest to predict inkjet printer source using Raman spectroscopy. Both examples are high consequence applications, where it is important to provide reasoning for the predictions for the models to be trusted to make decisions. The models selected for these analyses are selected as examples of two different commonly used black-box machine learning models. The data in these examples are available upon request, and the code is available at github.com/sandialabs/veesa/tree/master/demos/goode-et-al-paper.

4.1. *Hyperspectral Computed Tomography Data Material Classification .* Hyperspectral computed tomography (H-CT) scans of materials produce a signature across a set of frequencies unique to an observation. There is interest in using H-CT scans to identify explosives from a set of materials for applications such as airport security (Jimenez et al., 2017; Gallegos et al., 2018). In this example, we consider a set of 1,980,409 H-CT scans simulated by experts at Sandia National Laboratories that contain five materials: water (H_2O), hydrogen peroxide (H_2O_2) solutions diluted by water with 100%, 50%, and 10% H_2O_2 , and an explosive (Gallegos et al., 2019). The percentages of observations per material are 34%, 17%, 8%, 7%, and 34%, respectively. The signatures are separated into training and testing sets by randomly sampling 80% of scans from each material to be included in the training data. The top row of Figure 5 shows subsets of 1,000 randomly selected signatures per material from the training data. The scans record observations at 128 frequencies, which are visualized as normalized frequencies between 0 and 1.

We apply the VEESA pipeline with a neural network as the model to predict the material of an H-CT scan. Smoothing is performed using a box-filter. The number of times the box

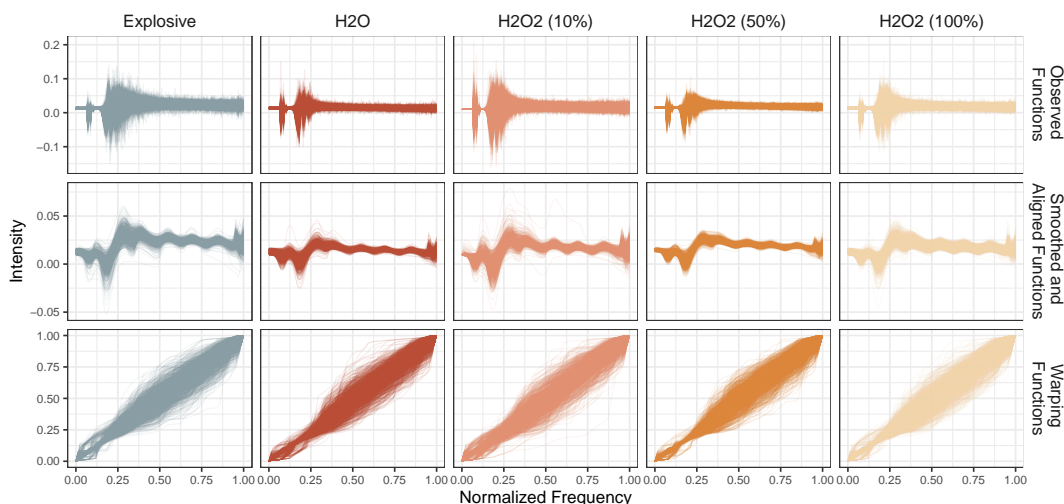


FIG 5. Observed (top row), smoothed and aligned (middle row), and warping functions (bottom row) of a subset of 1,000 H-CT signatures for each material.

filter is run (15 times) is determined by considering a range of values and selecting the value with the best predictive performance on the test data. The details of the smoothing process are included in the supplemental material. Figure 5 (middle and bottom rows) shows the subset of 1,000 signatures after smoothing and alignment and the corresponding warping functions.

As an exploratory analysis step, we compute the cross-sectional means of the aligned signatures for each material and the Karcher means of the warping functions for each material (Figure 6). The aligned means show clear vertical variability between the materials, and the pattern in vertical variability changes just before the normalized frequency of 0.25. For example, water and the explosive have similar intensities before a normalized frequency of 0.25. After the change, the explosive has the highest intensity, and water has the lowest intensity. There are minimal differences between the warping function material means, which indicates there is little horizontal variability between the H-CT functions, on average.

The trends in Figure 6 suggest that the characteristics in the data for discriminating between materials is likely captured in the vertical variability. As a result, we hypothesize that vfPCA will be a better option for discriminating between materials, but we also consider jfPCA in case there is discriminatory information in the horizontal variability that is not captured by the means. We train two models: one with vfPCs as inputs and one with jfPCs as inputs. For both models, all 128 PCs are included. The models are trained using the Python package *scikit-learn* (Pedregosa et al., 2011) with all default values (i.e., one layer with 100 neurons and a ReLU activation function). We elect to not perform model tuning for this analysis since PFI provides insight into a model regardless of whether it has good or bad predictive performance. Instead, we fit these two models and work to understand how they make use of the data. Additional work could be done to use information gained from this initial application of the VEESA pipeline to improve a model. PFI is applied to the test data using 5 replications and a performance metric of accuracy. A comparison of applications of the VEESA pipeline with a cross-sectional approach is included in the supplemental material.

Figure 7 shows the proportion of variation and PFI value associated with the jfPCs (left) and vfPCs (right). The variability across PFI replicates is not depicted since it is much smaller than the variability across PCs; see the supplemental material for more details on the variability. For both the vfPCA and jfPCA models, the proportion of variation has a major drop after the first PC and drops close to zero after a small number of PCs. In contrast, there is a much

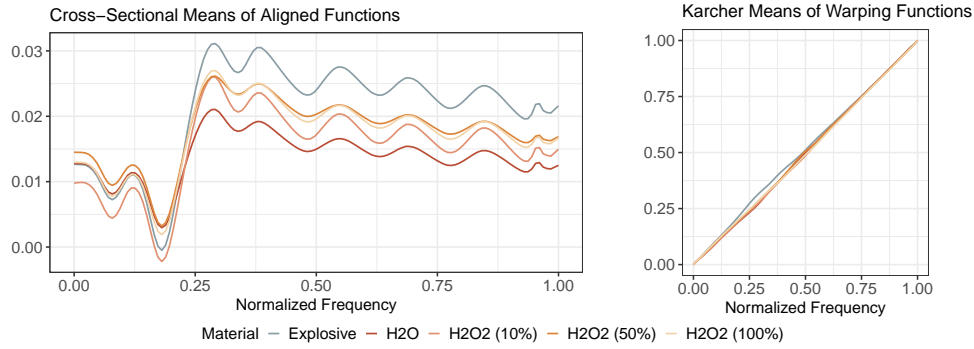


FIG 6. (Left) Cross-sectional functional means of the aligned functions in Figure 5 for each material. (Right) Karcher means of the warping functions within each material.

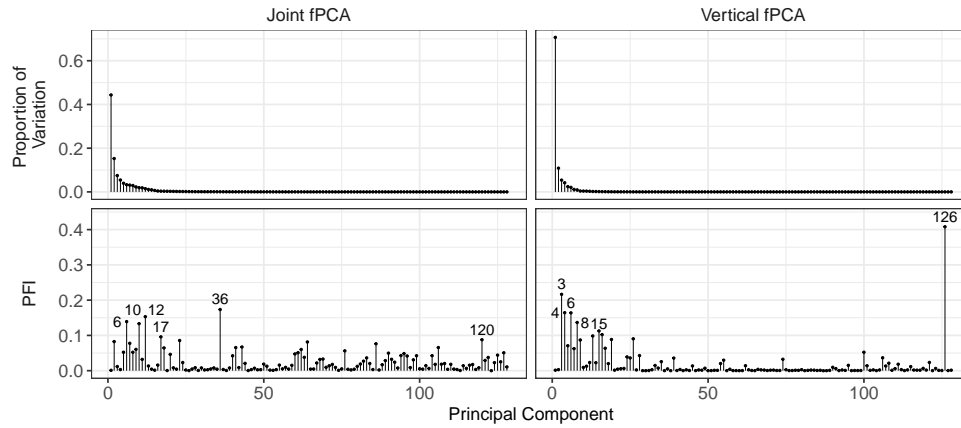


FIG 7. Proportion of variation (top) and PFI values (bottom) associated with the *jfPCs* (left) and *vfPCs* (right) in the H-CT example. The four *jfPCs* and *vfPCs* with the highest PFI are labeled.

different relationship between PFI values and principal component number, which provides a clear example where predictive value of a principal component is not directly related to the amount of variability explained by a principal component. For the *vfPCs*, PC 126 has an extremely high PFI value and a handful of earlier PCs have elevated PFI values. With the *jfPCs*, 4 PCs (before PC 50) stand out with PFI values higher than 0.1.

As expected, the model fit with *vfPCs* returns a higher test data accuracy of 0.88 compared to the model fit with *jfPCs* with a test data accuracy of 0.81. We consider some of the principal directions from the better performing *vfPC* model here and include principal directions from the *jfPC* model in the supplemental material. Figure 8 depicts the principal direction plots of the 6 *vfPCs* with the highest PFI values (i.e., the PCs with PFI values above 0.1). The PC with the highest PFI (*vfPC* 126) captures a consistent vertical variability across all frequencies. The other five *vfPCs* capture more nuanced aspects of the variability. *vfPC* 3 captures the contrast in intensities before and after frequency 0.25. *vfPC* 4 focuses on scans with low intensities around frequencies of 0.2 and 0.35 and above average intensities after 0.35. *vfPCs* 6, 8, and 15 all capture the change in intensities before and after 0.2 with slight different focuses: *vfPC* 6 focuses on the first peak after 0.2, *vfPC* 8 considers functions close to the mean function between approximately 0.2 and 0.3, and *vfPC* 15 considers functions close to the mean function between approximately 0.7 and 0.85.

The most important *vfPCs* appear to capture characteristics in the H-CT data that are reasonable given the clear distinction between the aligned material means in Figure 6. This is

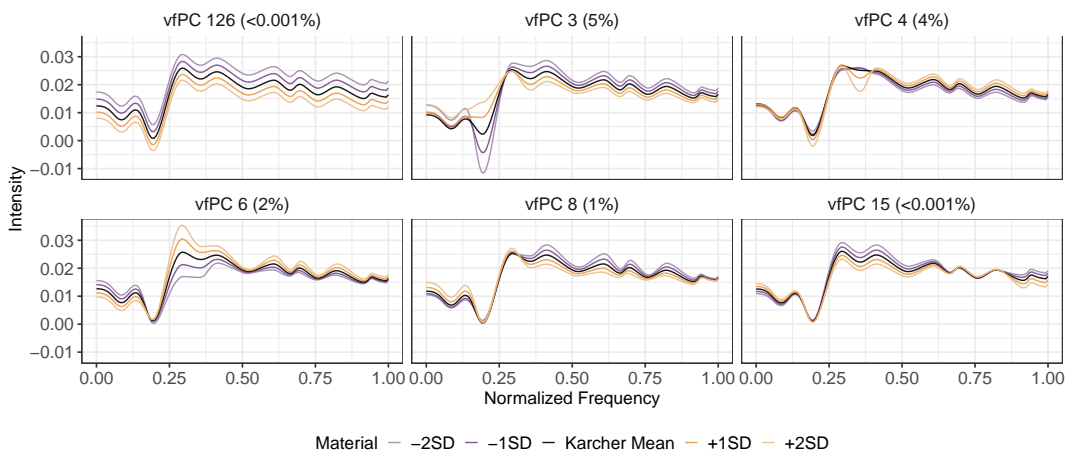


FIG 8. Principal directions from the six vfPCs with the highest PFI from the H-CT data example.

a promising start for an analysis of the H-CT. Next steps could involve removing vfPCs with PFI values close to 0 and model hyperparameter tuning to see if test data accuracy improves.

4.2. *Inkjet Printer Identification with Raman Spectroscopy*. Inkjet printers can be used for illicit activities such as printing counterfeit currency. As a result, forensic investigators are interested in techniques that provide evidence connecting printed material to the source printer. Buzzini, Curran and Polston (2021) present one approach where Raman spectroscopy is used to extract signatures from documents generated by inkjet printers. The authors then use different variants of linear discriminant analysis (LDA) to predict the source printer given a sample of Raman spectra, which we will refer to as a signature. Figure 9 shows signatures from different printers that Buzzini, Curran and Polston (2021) considered for their analyses. We will refer to this set of samples as the *inkjet dataset*. Since the Raman spectra signatures are functional data, we are interested in applying the VEESA pipeline to predict the source printer for a document given a Raman spectra signature and understand the functional variability important to the model for prediction.

The inkjet dataset (Figure 9) contains signatures collected from eleven documents belonging to the Counterfeit Forensic Section of the Criminal Investigative Division of the US Secret Service. Each document is printed from a different device, but some of the devices have the same manufacturer as shown in Table 2. In addition to sharing a manufacturer, printers 7 and 8 also are the same model of printer. For each document, 7 replicates were collected from the three main colored dot components (cyan, magenta, and yellow). Each replicate signature contains observations at 231 spectra between 1800 and 250 cm^{-1} . Buzzini, Curran and Polston (2021) converted the replicates to have 1129 observations per signature with a path of approximately 1.4 cm^{-1} . See Buzzini, Curran and Polston (2021) for more details on the collection process.

We choose to implement the VEESA pipeline using jfPCA since Figure 9 shows that there is variability in both the vertical and horizontal directions in the signatures, and we do not have prior knowledge of which type of variability contains information useful for prediction. Buzzini, Curran and Polston (2021) compare various preprocessing methods applied to the signatures before applying LDA. Their preprocessing steps included a baseline correction and different forms of normalization. We elect to only implement a box-filter for the smoothing step in the VEESA pipeline for preprocessing the functions before applying jfPCA. The variability removed by a baseline correction and normalization should be captured by the the jfPCs, and then the model should identify which modes of variability captured by the jfPCs

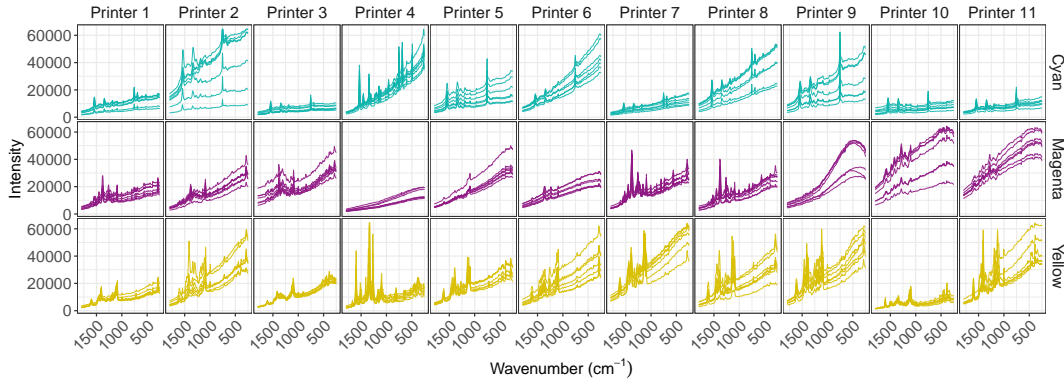


FIG 9. Raman spectra signatures from 11 inkjet printers for the colors of cyan, magenta, and yellow.

are useful for prediction. We are interested in determining if we can achieve equal or better performance without preprocessing.

We select a random forest as the predictive model as an example of commonly used statistical learning model. We follow a similar set up as [Buzzini, Curran and Polston \(2021\)](#) for the model predictive assessment, so we can compare our model performance to their best performing models. Specifically, we build predictive models separately for each color, and we implement a 3-fold cross validation procedure for predictive performance assessment. The folds are created such that each replicate for a printer and color is randomly assigned to be in fold 1, 2, or 3 (with 3 functions in fold 1 and 2 functions in folds 2 and 3). Then two of the folds are used to train a model using Steps 1-4 of the VEESA pipeline described in Section 3.1, and the third fold is used for testing Steps 1-4 of the VEESA pipeline described in Section 3.2. The procedure is repeated such that the three possible fold pairs are used for training. Since the fold a signature is assigned to is random, this 3-fold cross validation procedure is repeated a total of 10 times to account for variability.

Table 2: Printer manufactures and models in the inkjet dataset.

Printer	Manufacturer	Model
1	Brother	MFC-665CW
2	Canon Pixma	MX340
3	Canon PG	210XL
4	Epson	Unknown
5	HP	Officejet 5740
6	HP	Deskjet f5180
7	HP	Officejet 6500
8	HP	Officejet 6500
9	Lexmark	228 2010 CE 81
10	Sensient	Unknown
11	Sensient	Unknown

For each color, model accuracy is computed for each test fold and repetition, and the cross validation predictive performance metric is computed as the average of the test-fold accuracies across the 10 replicates. That is, let y_i represent the true printer associated with observation $i = 1, \dots, 77$, and let $\hat{y}_{i,r}$ represent the predicted value of y_i when observation i is

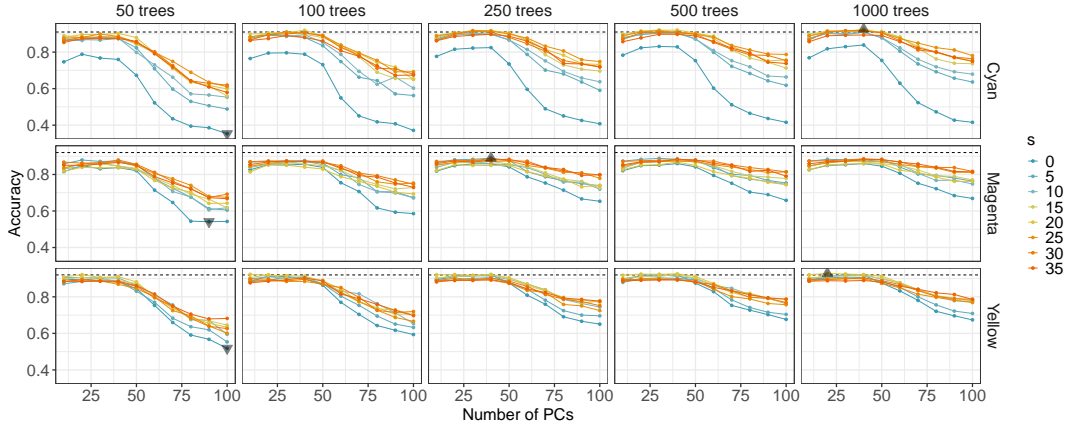


FIG 10. Cross validation average accuracies. Triangles pointing up and down highlight the highest and lowest average cross validation accuracies from the VEESA pipeline, respectively, for each color. Horizontal dashed lines represent best average cross validation accuracies for each color from Buzzi, Curran and Polston (2021).

in the test fold for replicate $r = 1, \dots, 10$. The cross validation average accuracy for one color ($color \in \{\text{cyan, magenta, yellow}\}$) is computed as

$$Acc_{color} = \frac{1}{10 \cdot 77} \sum_{r=1}^{10} \sum_{i=1}^{77} I[y_i = \hat{y}_{(i,r)}].$$

There are a handful of values that must be specified when implementing the VEESA pipeline. We choose to vary the number of times the box-filter is run for smoothing (0, 5, 10, 15, 20, 25, 30, and 35 times), the number of PCs input to the model (10, 20, 30, 40, 50, 60, 70, 80, 90, and 100 PCs), and the number of trees in the random forest (50, 100, 250, 500, and 1000 trees). The cross validation process is applied 400 times for each color (once for all combinations of box-filter runs, input PCs, and random forest trees). The values considered are selected to show a range over which model accuracy increases and diminishes. The random forests are fit using the *randomForest* R package (Liaw and Wiener, 2002) with all tuning parameters set to the default value besides for the number of trees.

The cross validation average accuracies are shown in Figure 10. The x-axis shows the number of PCs input to the model, and the y-axis depicts the cross validation accuracy. The rows and columns separate the results by color and the number of random forest trees, respectively. The color of a line represents the number of times the box filter is run, and the horizontal dashed black line represents the best cross validation accuracy for a color obtained by Buzzi, Curran and Polston (2021). There are some clear trends in the cross validation results. For example, regardless of the number of random forest trees, the average accuracies tend to increase as the number of PCs increases to around 30-50 and then decrease as the number of PCs increase further. We also see that for all PCs, number of trees, and color, the more times the box-filter is run, the average accuracy tends to increase until approximately 25 times when the improvement is either minimal or the accuracy begins to decrease.

The grey triangles pointing up and down in Figure 10 indicate the VEESA pipeline scenarios with the highest and lowest average cross validation accuracy, respectively, within a color. Table 3 contains the number values of the highest and lowest CV averaged accuracies associated with the triangles in Figure 10. The values associated with the VEESA pipeline implementation that results in these values are also included (i.e., number of PCs, number of trees, and smoothing iterations). Note that the lowest accuracies from the VEESA pipeline have no smoothing and many PCs. For cyan and yellow, we achieve approximately the same

or better predictive performance. For magenta, our highest average cross validation accuracy is close but lower. Additional investigations show that the low magenta accuracy with the VEESA pipeline is due to printers 7 and 8 being classified as the other printer. These two printers have the same manufacturer and model, and Figure 9 shows that their signatures similar. Additional details about individual printer classifications are included in the supplemental material.

Table 3: Cross validation average accuracies from the best and worst performing VEESA pipeline models applied to the inkjet dataset. The last column contains the highest cross validation accuracies achieved by [Buzzini, Curran and Polston \(2021\)](#).

Scenario	Color	Box Filter	PCs	Trees	VEESA	Buzzini
Best	Cyan	20	40	1000	0.9260	0.91
Best	Magenta	5	40	250	0.8896	0.92
Best	Yellow	20	20	1000	0.9286	0.92
Worst	Cyan	0	100	50	0.3532	-
Worst	Magenta	0	90	50	0.5416	-
Worst	Yellow	0	100	50	0.5182	-

For each of the best and worst performing tuning parameter scenarios, we train a random forest on the data from all printers. Again, the models are trained separately for each color. We elect to train these models on all data within a color to mimic the joining of all available data to build a model for predictions on new data without a known printer. We apply the VEESA pipeline to understand how such a model makes use of the functional variability in the inkjet signatures. We choose to consider both the best and worst cases to study how the feature importance varies between good and poor performing models.

When implementing the VEESA pipeline with all signatures for a color, we apply all steps described in Section 3.1 with jfPCA. We compute PFI for the jfPCs using 10 replications. The PFI results are included in Figure 11. The best performing models place high importance on the earlier PCs, and the worst performing models place importance on both early PCs and later PCs (i.e., the PCs with high are either less than 15 or greater than 75). The low importance of PCs 15 to 75 suggest that they may be able to be removed to improve model predictive performance of the worst performing scenarios. We explore how the removal of these PCs affects the model accuracies in the supplemental material.

Figure 12 shows principal directions from the best and worst performing models for cyan signatures. For space reasons, we only consider the five PCs with the highest feature importance values. We start by considering the important principal directions associated with the best model (Figure 12 top). While there are nuances in the variability captured, jfPCs 1, 2, and 3 generally capture vertical variability with increasing variability as the wavenumber approaches 500. Each of these PCs also captures small amounts of horizontal variability. For example, the most important PC, jfPC 3, captures small amounts of horizontal variability in the first two main peaks that occur at larger wavenumbers than the mean. For the third peak, jfPC 3 captures variability in functions that peak before and after the mean. jfPC 7 consistently captures approximately the same amount of vertical variability across wavenumbers. Lastly, jfPC 5 captures small amounts of vertical variability before and after the third main peak. It seems reasonable that the model would focus on these modes of variability for prediction. In Figure 9, a key distinguishing factor between printers in cyan signatures is the different in the slope of the intensity values as the wavenumbers approach 500 cm^{-1} . Another

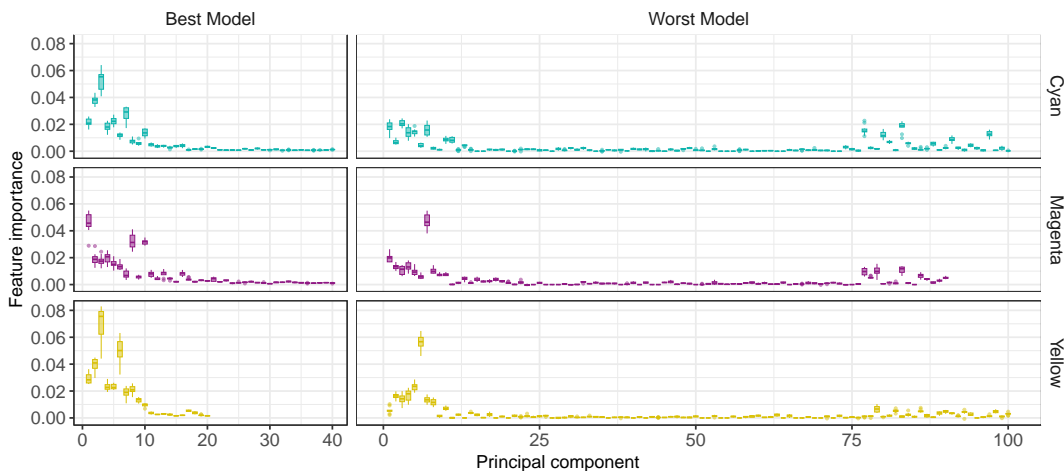


FIG 11. Boxplots of PFI values across 10 replications from the best and worst performing models for cyan, magenta, and yellow inkjet signatures.

distinguishing factor is the height of the main three peaks and small amounts of variability in the wavenumbers where the main peaks occur.

The most important jfPCs for the worst performing model capture similar aspects of functional variability as the best performing model. In fact, the jfPCs of 1, 3, and 7 appear again. Even though no smoothing is applied to the signatures with this model, the larger picture functional variability matches that captured by the jfPCs with the same numbers. However, these PCs are clearly less smooth. The other two important jfPCs that fall in the top five (jfPCs 77 and 83) capture such little variability that it is not visible in these figures. Instead, these capture variability in functions that are similar to the mean, versus those that are not. It is possible that information could be useful for classification (i.e., some of the printer signatures in Figure 9 are similar to the Karcher mean and some are very different). However, the additional noise in the functions when no smoothing is applied must make it difficult to separate key characteristics of the signatures that are unique to a printer.

The principal directions associated with the most important PCs for the best and worst magenta and yellow models are included in the supplemental material. Overall, we are able to achieve similar predictive performance as the analysis in [Buzzini, Curran and Polston \(2021\)](#) while additionally gaining insight into how the random forests make use of patterns in the data. We are able to achieve this predictive performance without as much preprocessing of the data as implemented in the analysis of [Buzzini, Curran and Polston \(2021\)](#). We point this out, because this also highlights that the VEESA pipeline could be beneficial for analyses that do not have access to subject matter experts or scenarios where it is not previously understood how to best preprocess the data based on prior experiences.

5. Discussion . While there has been much research on explainable machine learning, there is little research that specifically considers functional data as model inputs and accounts for the dependence structure in the data. The VEESA pipeline provides a way for model developers to train a supervised machine learning model with functional data inputs that (1) accounts for functional dependence and the horizontal and vertical functional variability of functional data inputs and (2) identifies the aspects of functional variability that are globally important to the model. This is done by first applying some pre-processing steps: the functions are smoothed, the horizontal and vertical variability in the functions are separated using the ESA framework, and efPCA is applied. Then a machine learning model is trained

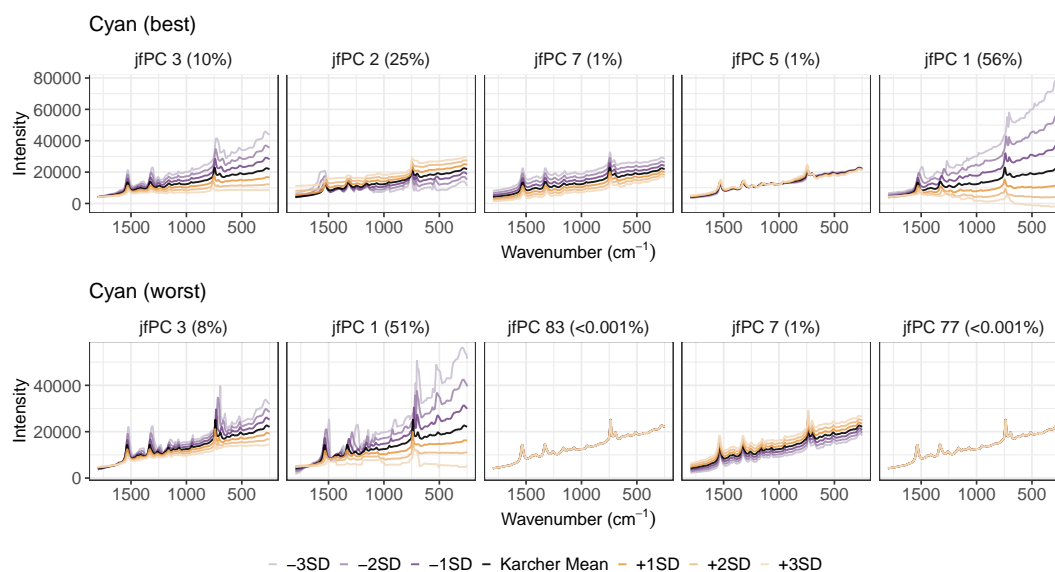


FIG 12. Principal directions from the best (top row) and worst (bottom row) models for predictions with cyan inkjet signatures. The jfPCs selected are those with the largest PFI values for their respective model. PCs are ordered from left to right based on highest to lowest feature importance.

with the efPCs as the predictor variables, and PFI is used to identify the efPCs important for prediction. Finally, the principal directions of the important efPCs are visualized to interpret the functional variability captured. The process may also be applied to test data to gain insight into how the model produces predictions on data not seen during training. The VEESA pipeline offers one approach to explainable machine learning with functional data, but this approach is only a start. There are numerous directions for improvement and future research.

An important element to consider, as previously discussed, is the nature of explanations is dictated by the intended audience. The VEESA pipeline is aimed at providing insight to model developers and, potentially, subject matter experts. However, if a model developed using the VEESA pipeline is deployed, additional steps should be taken to determine the form of explanations aimed at users or decision makers who do not possess the same technological knowledge as the model developers or subject matter experts. The manner in which a model would be used in practice could take different forms. For example, in the inkjet analysis, a model developer may apply the model to a new prediction that could be used in a court case, but the developer may need to be creative to find a way to distill their understanding of what is important to the model to provide explanations to lawyers, judges, and juries. In the H-CT material classification, consider the scenario where a model developed with the VEESA pipeline is used by airport security to scan luggage for explosives. Simply providing the global PFI values will not be sufficient to help the security employees trust and work with the model. Instead, an interactive tool that allows the employees to explore understandable explanations for individual predictions (i.e., local instead of global explanations) would be more valuable (e.g., Wang et al. (2022)). In general, there is much room for the advancement of explanations intended for decision makers as highlighted by Bhatt et al. (2020).

As briefly mentioned in the previous paragraph, there are two types of explanations: global and local. Global explanations aim to provide a summary of how a model makes use of data across an entire set of predictions. Local explanations aim to provide reasoning for how a model makes use of data for an individual prediction. PFI is a global explanation technique. Other types of global explanations include partial dependence plots (PDPs) (Friedman, 2001) and global surrogate models (Molnar, 2022). Local methods include individual conditional

expectation (ICE) plots ([Alex Goldstein and Pitkin, 2015](#)) and SHAP ([Lundberg and Lee, 2017](#)). Any of these or other explainability techniques could be used in place of PFI in the VEESA pipeline. For example, PDPs would provide a visual of the average marginal relationships between the predictions and the efPCs. ICE plots would provide the same visual but for individual predictions. Arguably, the best route would be to draw on the explainability tool box and apply multiple methods to gain different perspectives into the model. In addition to efPCs accounting for both types of variability present in functional data, the use of efPCs provides an additional advantage to using other explainability methods. Just as PFI is known to provide biased results when correlation is present between variables, PDPs, ICE plots, SHAP, and other explainability techniques are also known to be negatively affected by correlation between predictor variables ([Molnar et al., 2020](#); [Hooker, Mentch and Zhou, 2021](#)). Since the efPCs are uncorrelated, explainability methods known to be negatively affected by correlation are able to be applied without concern due to correlation.

There are also various directions for research specific to PFI. We describe these topics in the context of the VEESA pipeline, but the ideas apply more generally. If PFI returns a large number of efPCs with significant importance, there may be too much information for analysts to extract a clear understanding. Future work could investigate an index for specifying whether a model has high or low explainability potentially based on the number of important features and their usefulness. Such a metric could help determine what level of deployment a model is ready for depending on the consequential nature of the application. Additionally, future work could investigate a method for determining a “cut off” for which efPCs are considered important, which could be useful for feature selection (i.e., remove the unimportant or less important efPCs, retrain the model, and determine if interpretability is improved with fewer efPCs while maintaining or improving on predictive performance).

Another issue is the computational intensity of PFI. For large machine learning data sets, the process of applying PFI to a dataset may need to be adjusted. One route may be to select a subset that is representative of the data of interest that PFI is applied to. A survey sampling method may be applicable here. Instead of a representative sample, a subset could also be chosen based on observations of interest, which may provide valuable insight to a model regardless of the data size. For example, PFI could be applied separately to clusters identified in the data, only observations that are predicted incorrectly by the model, or separately by classes. Considering feature importance separately by class may be of special interest in the case of uneven class sizes. A different route to take with large datasets to apply PFI to all observations would be to break the computation into pieces that could be implemented independently and later combined. Other areas of active research with feature importance include quantifying variable interactions (e.g., [Greenwell, Boehmke and McCarthy \(2018\)](#)) and computing uncertainty (e.g., [Brian D. Williamson and Carone \(2023\)](#)).

There are several unspoken assumptions underlying the VEESA pipeline that should be addressed. First, we assume that the efPCs have meaningful contextual interpretations. If the efPCs are difficult to interpret, then it will not be clear what aspects of the functional variability are driving the model predictions. A way to resolve this issue is to use a different method for summarizing the functions while appropriately accounting for their variability such as a varimax rotation ([Ramsay and Silverman, 2005](#)). It may also be possible to substitute efPCA with a different method that accounts for both the horizontal and vertical variability, is interpretable, and provides uncorrelated variables. Some possible methods include partial least squares (PLS) for functional data ([Febrero-Bande, Galeano and González-Manteiga, 2017](#)) and canonical correlation analysis ([Lee, 2017](#)).

The second assumption we make is that the only inputs to the model are efPCs from one set of functions. If there are additional variables (e.g., individual vectors or efPCs from another set of functions), the guarantee of uncorrelated input variables may no longer hold.

For example, in the inkjet analysis, a clear next step is to train a model including all three colors. However, if the efPCs computed separately on cyan, magenta, and yellow signatures are included, the PFI may be biased. There is some work on computing feature importance that accounts for correlation between input variables (e.g., Strobl et al. (2008) and Hooker, Mentch and Zhou (2021)), but this is another area of active research.

The final assumption is that the approach for implementing efPCA described in this paper assumes that the functions have the same number of peaks. If the functions have different numbers of peaks, the approach has to decide which nearby peak to align a function with, which could affect classification. Future work could explore the use of a Bayesian multimodal alignment approach that has been proposed for handling this scenario under the ESA framework (Tucker, Shand and Chowdhary, 2021).

The VEESA pipeline is an example of a procedure that combines methods commonly thought of as “statistical” methods (efPCA) with machine learning approaches (PFI). By joining statistical and machine learning approaches, the pipeline takes advantage of the benefits of both: the ability to capture the data dependence structure with efPCA and the data driven predictive ability of machine learning. We echo previous authors that are encouraging more meshing of the two cultures in hopes of the development of new approaches that draw on the benefits of the two approaches.

Acknowledgments. The authors thank Danica Ommen for pointing us to the inkjet application and Patrick Buzzinni for providing us access to the inkjet data. Additionally, we thank Philip Kegelmeyer for a careful reading of the manuscript and insightful feedback.

Funding. Sandia National Laboratories is a multimission laboratory managed and operated by National Technology & Engineering Solutions of Sandia, LLC, a wholly owned subsidiary of Honeywell International Inc., for the U.S. Department of Energy’s National Nuclear Security Administration under contract DE-NA0003525. This paper describes objective technical results and analysis. Any subjective views or opinions that might be expressed in the paper do not necessarily represent the views of the U.S. Department of Energy or the United States Government. SAND2025-000080.

REFERENCES

- ADADI, A. and BERRADA, M. (2018). Peeking Inside the Black-Box: A Survey on Explainable Artificial Intelligence (XAI). *IEEE Access* **6** 52138–52160. <https://doi.org/10.1109/access.2018.2870052>
- ALEX GOLDSTEIN, J. B. ADAM KAPELNER and PITKIN, E. (2015). Peeking Inside the Black Box: Visualizing Statistical Learning With Plots of Individual Conditional Expectation. *Journal of Computational and Graphical Statistics* **24** 44–65. <https://doi.org/10.1080/10618600.2014.907095>
- BARINDER THIND, K. M. and CAO, J. (2023). Deep Learning With Functional Inputs. *Journal of Computational and Graphical Statistics* **32** 171–180. <https://doi.org/10.1080/10618600.2022.2097914>
- BERTSEKAS, D. P. (1996). Dynamic programming and optimal control. *Journal of the Operational Research Society* **47** 833–833.
- BHATT, U., XIANG, A., SHARMA, S., WELLER, A., TALY, A., JIA, Y., GHOSH, J., PURI, R., MOURA, J. M. and ECKERSLEY, P. (2020). Explainable machine learning in deployment. In *Proceedings of the 2020 conference on fairness, accountability, and transparency* 648–657.
- BREIMAN, L. (2001). Random Forests. *Machine Learning* **45** 5–32. <https://doi.org/10.1023/a:1010933404324>
- BRIAN D. WILLIAMSON, N. R. S. PETER B. GILBERT and CARONE, M. (2023). A General Framework for Inference on Algorithm-Agnostic Variable Importance. *Journal of the American Statistical Association* **118** 1645–1658. PMID: 37982008. <https://doi.org/10.1080/01621459.2021.2003200>
- BUTTS-WILMSMEYER, C. J., RAPP, S. and GUTHRIE, B. (2020). The technological advancements that enabled the age of big data in the environmental sciences: A history and future directions. *Current Opinion in Environmental Science and Health* **18** 63–69. Environmental Chemistry: Innovative Approaches and Instrumentation in Environmental Chemistry. <https://doi.org/10.1016/j.coesh.2020.07.006>

- BUZZINI, P., CURRAN, J. and POLSTON, C. (2021). Comparison between visual assessments and different variants of linear discriminant analysis to the classification of Raman patterns of inkjet printer inks. *Forensic Chemistry* **24** 100336.
- DANNE, T., NIMRI, R., BATTELENO, T., BERGENSTAL, R. M., CLOSE, K. L., DEVRIES, J. H., GARG, S., HEINEMANN, L., HIRSCH, I., AMIEL, S. A., BECK, R., BOSI, E., BUCKINGHAM, B., COBELLI, C., DASSAU, E., DOYLE, F. J., HELLER, S., HOVORKA, R., JIA, W., JONES, T., KORDONOURI, O., KOVATCHEV, B., KOWALSKI, A., LAFFEL, L., MAAHS, D., MURPHY, H. R., NØRGAARD, K., PARKIN, C. G., RENARD, E., SABOO, B., SCHARF, M., TAMBORLANE, W. V., WEINZIMER, S. A. and PHILLIP, M. (2017). International Consensus on Use of Continuous Glucose Monitoring. *Diabetes Care* **40** 1631–1640. <https://doi.org/10.2337/dc17-1600>
- FEBRERO-BANDE, M., GALEANO, P. and GONZÁLEZ-MANTEIGA, W. (2017). Functional Principal Component Regression and Functional Partial Least-squares Regression: An Overview and a Comparative Study. *International Statistical Review* **85** 61–83. <https://doi.org/10.1111/insr.12116>
- FISHER, A., RUDIN, C. and DOMINICI, F. (2019). All Models are Wrong, but Many are Useful: Learning a Variable’s Importance by Studying an Entire Class of Prediction Models Simultaneously. *Journal of Machine Learning Research* **20** 1–81.
- FRIEDMAN, J. H. (2001). Greedy function approximation: A gradient boosting machine. *The Annals of Statistics* **29**. <https://doi.org/10.1214/aos/1013203451>
- GALLEGOS, I. O., KOUNDINYAN, S., SUKNOT, A. N., JIMENEZ, E. S., THOMPSON, K. R. and GOODNER, R. N. (2018). Unsupervised learning methods to perform material identification tasks on spectral computed tomography data. In *Radiation detectors in medicine, industry, and national security XIX* **10763** 91–104. SPIE.
- GALLEGOS, I. O., DALTON, G. M., STOHN, A. M., KOUNDINYAN, S. P., THOMPSON, K. R. and JIMENEZ, E. S. (2019). High-fidelity calibration and characterization of a spectral computed tomography system. In *Hard X-Ray, Gamma-Ray, and Neutron Detector Physics XXI* **11114** 223–236. SPIE.
- GOODE, K., RIES, D. and ZOLLWEG, J. (2020). Explaining Neural Network Predictions for Functional Data Using Principal Component Analysis and Feature Importance. In *Proceedings of the Association for the Advancement of Artificial Intelligence (AAAI) Fall Symposium Series 2020: Artificial Intelligence in Government and Public Sector*.
- GOODE, K. and TUCKER, J. D. (2024). veesa: VEESA Pipeline for Explainable Machine Learning with Functional Data R package version 0.1.2.
- GREENWELL, B. M., BOEHMKE, B. C. and MCCARTHY, A. J. (2018). A simple and effective model-based variable importance measure. arXiv. Unpublished manuscript.
- GUIDOTTI, R., MONREALE, A., RUGGIERI, S., TURINI, F., GIANNOTTI, F. and PEDRESCHI, D. (2018). A Survey of Methods for Explaining Black Box Models. *ACM Computing Surveys (CSUR)* **51** 42 pages. <https://doi.org/10.1145/3236009>
- HENRIKSEN, A., HAUGEN MIKALSEN, M., WOLDAREGAY, A. Z., MUZNY, M., HARTVIGSEN, G., HOPSTOCK, L. A. and GRIMSGAARD, S. (2018). Using Fitness Trackers and Smartwatches to Measure Physical Activity in Research: Analysis of Consumer Wrist-Worn Wearables. *J Med Internet Res* **20** e110. <https://doi.org/10.2196/jmir.9157>
- HOOKE, G., MENTCH, L. and ZHOU, S. (2021). Unrestricted permutation forces extrapolation: variable importance requires at least one more model, or there is no free variable importance. *Statistics and Computing* **31** 1–16.
- JIMENEZ, E. S., THOMPSON, K. R., STOHN, A. and GOODNER, R. N. (2017). Leveraging multi-channel x-ray detector technology to improve quality metrics for industrial and security applications. In *Radiation Detectors in Medicine, Industry, and National Security XVIII* **10393** 137–147. SPIE.
- JOSHI, S. H., KLASSEN, E., SRIVASTAVA, A. and JERMYN, I. (2007). A Novel Representation for Riemannian Analysis of Elastic Curves in Rn. *2007 IEEE Conference on Computer Vision and Pattern Recognition* 1–7. <https://doi.org/10.1109/cvpr.2007.383185>
- LEE, S. (2017). Integrative Analysis of Variation Structure in High-dimensional Multi-block Data, PhD thesis, University of Pittsburgh, Pittsburgh, PA Supervised by Sungkyu Jung.
- LI, H., XIAO, G., XIA, T., TANG, Y. Y. and LI, L. (2014). Hyperspectral Image Classification Using Functional Data Analysis. *IEEE Transactions on Cybernetics* **44** 1544–1555. <https://doi.org/10.1109/TCYB.2013.2289331>
- LIAW, A. and WIENER, M. (2002). Classification and Regression by randomForest. *R News* **2** 18–22.
- LUNDBERG, S. M. and LEE, S.-I. (2017). A unified approach to interpreting model predictions. *Advances in neural information processing systems* **30**.
- MARTIN-BARRAGAN, B., LILLO, R. and ROMO, J. (2014). Interpretable support vector machines for functional data. *European Journal of Operational Research* **232** 146–155. <https://doi.org/10.1016/j.ejor.2012.08.017>

- MOLNAR, C. (2022). *Interpretable Machine Learning*, 2 ed.
- MOLNAR, C., CASALICCHIO, G. and BISCHL, B. (2020). Interpretable Machine Learning – A Brief History, State-of-the-Art and Challenges. In *ECML PKDD 2020 Workshops* (I. KOPRINSKA, M. KAMP, A. APPICE, C. LOGLISCI, L. ANTONIE, A. ZIMMERMANN, R. GUIDOTTI, Ö. ÖZGÖBEK, R. P. RIBEIRO, R. GAVALDÀ, J. GAMA, L. ADILOVA, Y. KRISHNAMURTHY, P. M. FERREIRA, D. MALERBA, I. MEDEIROS, M. CECI, G. MANCO, E. MASCIARI, Z. W. RAS, P. CHRISTEN, E. NTOUTSI, E. SCHUBERT, A. ZIMEK, A. MONREALE, P. BIECEK, S. RINZIVILLO, B. KILLE, A. LOMMATZSCH and J. A. GULLA, eds.) 417–431. Springer International Publishing, Cham.
- MOLNAR, C., KÖNIG, G., HERBINGER, J., FREIESLEBEN, T., DANDL, S., SCHOLBECK, C. A., CASALICCHIO, G., GROSSE-WENTRUP, M. and BISCHL, B. (2020). General pitfalls of model-agnostic interpretation methods for machine learning models. In *International Workshop on Extending Explainable AI Beyond Deep Models and Classifiers* 39–68. Springer.
- PEDREGOSA, F., VAROQUAUX, G., GRAMFORT, A., MICHEL, V., THIRION, B., GRISEL, O., BLONDEL, M., PRETTENHOFER, P., WEISS, R., DUBOURG, V., VANDERPLAS, J., PASSOS, A., COURNAPEAU, D., BRUCHER, M., PERROT, M. and DUCHESNAY, E. (2011). Scikit-learn: Machine Learning in Python. *Journal of Machine Learning Research* **12** 2825–2830.
- RAMSAY, J. O. and SILVERMAN, B. W. (2005). *Functional Data Analysis*, 2 ed. *Springer Series in Statistics* **0172-7397**. Springer - Verlag New York, Verlag, New York. <https://doi.org/10.1007/b98888>
- RIES, D. and GABRIEL HUERTA, J. (2023). Predicting fatigue from heart rate signatures using functional logistic regression. *Stat* **12** e595. <https://doi.org/10.1002/sta4.595>
- ROSSI, F., DELANNAY, N., CONAN-GUEZ, B. and VERLEYSEN, M. (2005). Representation of functional data in neural networks. *Neurocomputing* **64** 183–210. <https://doi.org/10.1016/j.neucom.2004.11.012>
- RUDIN, C. (2019). Stop explaining black box machine learning models for high stakes decisions and use interpretable models instead. *Nature Machine Intelligence* **1** 206–215. <https://doi.org/10.1038/s42256-019-0048-x>
- SRIVASTAVA, A. and KLASSEN, E. P. (2016). *Functional Shape and Data Analysis*. Springer Nature, New York.
- SRIVASTAVA, A., KLASSEN, E., JOSHI, S. H. and JERMYN, I. H. (2011). Shape Analysis of Elastic Curves in Euclidean Spaces. *IEEE Transactions on Pattern Analysis and Machine Intelligence* **33** 1415–1428. <https://doi.org/10.1109/TPAMI.2010.184>
- STROBL, C., BOULESTEIX, A.-L., KNEIB, T., AUGUSTIN, T. and ZEILEIS, A. (2008). Conditional variable importance for random forests. *BMC Bioinformatics* **9** 307. <https://doi.org/10.1186/1471-2105-9-307>
- TIAN, T. S. (2010). Functional Data Analysis in Brain Imaging Studies. *Frontiers in Psychology* **1** 35. <https://doi.org/10.3389/fpsyg.2010.00035>
- TUCKER, J. D. (2024a). fdasrvf: Elastic Functional Data Analysis R package version 2.2.0.
- TUCKER, J. D. (2024b). fdasrsf Python package version 2.4.2.
- TUCKER, J. D., LEWIS, J. R. and SRIVASTAVA, A. (2019). Elastic functional principal component regression. *Statistical Analysis and Data Mining: The ASA Data Science Journal* **12** 101–115. <https://doi.org/10.1002/sam.11399>
- TUCKER, J. D., SHAND, L. and CHOWDHARY, K. (2021). Multimodal Bayesian registration of noisy functions using Hamiltonian Monte Carlo. *Computational Statistics & Data Analysis* **163** 107298. <https://doi.org/10.1016/j.csda.2021.107298>
- TUCKER, J. D., WU, W. and SRIVASTAVA, A. (2013). Generative models for functional data using phase and amplitude separation. *Computational Statistics & Data Analysis* **61** 50–66. <https://doi.org/10.1016/j.csda.2012.12.001>
- TUCKER, J. D., LEWIS, J. R., KING, C. and KURTEK, S. (2020). A geometric approach for computing tolerance bounds for elastic functional data. *Journal of Applied Statistics* **47** 481–505. <https://doi.org/10.1080/02664763.2019.1645818>
- ULLAH, S. and FINCH, C. F. (2013). Applications of functional data analysis: A systematic review. *BMC medical research methodology* **13** 1–12.
- WANG, Z. J., KALE, A., NORI, H., STELLA, P., NUNNALLY, M. E., CHAU, D. H., VORVOREANU, M., WORTMAN VAUGHAN, J. and CARUANA, R. (2022). Interpretability, Then What? Editing Machine Learning Models to Reflect Human Knowledge and Values. In *Proceedings of the 28th ACM SIGKDD Conference on Knowledge Discovery and Data Mining. KDD '22* 4132–4142. Association for Computing Machinery, New York, NY, USA. <https://doi.org/10.1145/3534678.3539074>
- ZHANG, H. (2019). Topics in functional data analysis and machine learning predictive inference, PhD thesis 17626.
- ZHANG, Y. and CHEN, X. (2020). Explainable Recommendation: A Survey and New Perspectives. *Foundations and Trends® in Information Retrieval* **14** 1–101. <https://doi.org/10.1561/15000000066>

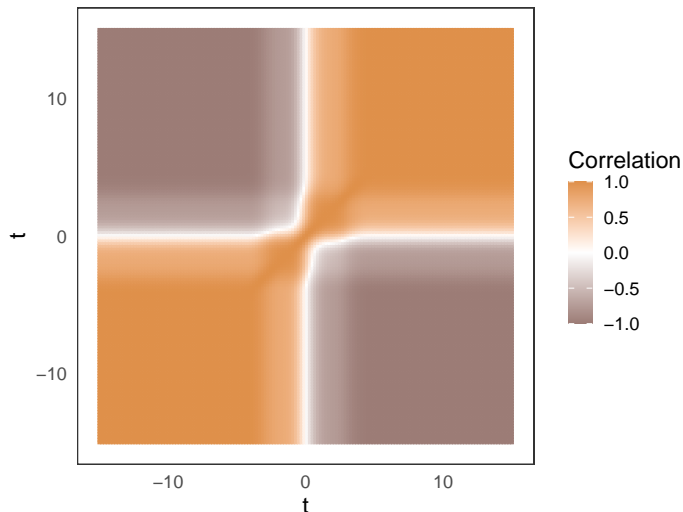


FIG 13. Spearman correlations between all pairs of cross-sectional variables from the simulated data.

Supplement

This document contains additional applications of the VEESA pipeline corresponding to the article “An Explainable Pipeline for Machine Learning with Functional Data”. Section 6 compares the VEESA pipeline to the cross-sectional approach with the simulated data. Section 7 contains additional details about the H-CT scan example. Lastly, Section 8 contains additional details about the inkjet printer example.

6. Comparing VEESA Pipeline to Cross-Sectional Approach with the Simulated Data. The cross-sectional approach treats the observations across functions at each time point as the predictor variables. An explainability method such as PFI may then be applied to try to identify the times that are important to the model for prediction. However, this approach presents a disadvantage. Due to the nature of functional data, the cross-sectional predictor variables are likely to be correlated. For example, consider the simulated described in Section 2 of the main text. Figure 13 shows a heatmap of all pairwise Spearman correlations between the cross-sectional simulated data predictor variables. There are strong positive and negative correlations for almost all variables. As mentioned in Section 1 of the main text, correlation between predictor variables leads to biased PFI results. Here, we apply the cross-sectional modeling approach to the simulated data and compare the results to the VEESA pipeline. We highlight the difficulties with gaining insight to the model produced by the cross-sectional approach.

The simulated data is separated in the same training and testing datasets with 400 and 100 observations, respectively. A random forest is trained on the training data (*randomForest* R package; version 4.7.1.1). The cross-sectional variables (one associated with each of the 150 times where the functions are observed) are treated as inputs. The observed group is the response variable. The default tuning parameters options are used to mimic the VEESA pipeline random forest from the main text. The random forest performs well on the test data with an accuracy of 1. The accuracy is slightly higher than the result from the VEESA pipeline random forest (0.99). PFI is applied to the test data using a metric of accuracy with 10 replications to mimic the computation of PFI in the VEESA pipeline from the main text.

Figure 14A includes the true group means depicted as solid lines and the cross-sectional group means depicted by points. The error bars represent plus/minus one cross-sectional

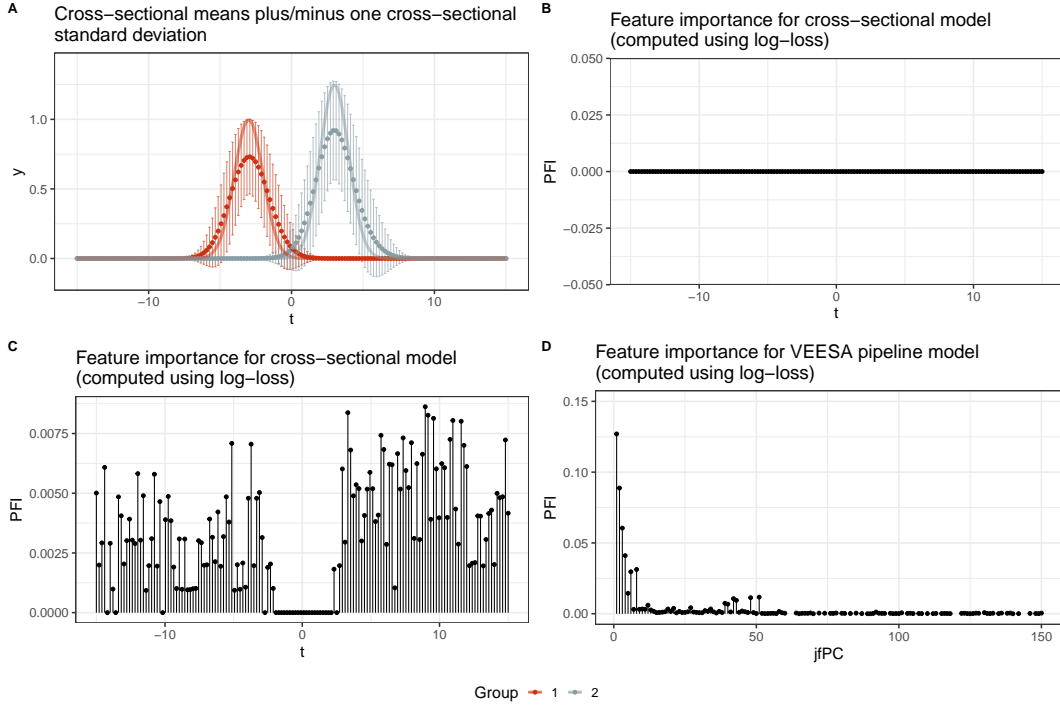


FIG 14. (A) The solid lines represent the true group means. The dots and error bars represent the cross-sectional group means plus and minus one cross-sectional standard deviation. (B-D) PFI values computed on the test data using the metric of accuracy for a random forest trained using the cross-sectional approach, using the metric of log-loss for a random forest trained using the cross-sectional approach, and the metric of log-loss for a random forest trained using the VEESA pipeline, respectively.

standard deviation. As seen in Section 2, the cross-sectional means do not capture the shape of the true means. Figure 14B depicts the PFI values computed using the cross-sectional approach. Unlike the PFI results from the VEESA pipeline method (Figure 3), the PFI values for all variables (time points in this instance) are approximately 0 with no variability (all times have standard deviations across PFI replicates of 0). In this instance, the PFI results do not appear to be inflated due to bias. Instead, this result suggests that none of the individual time points are important in regards to the accuracy of the model. These PFI results indicate that permuting one time point, while leaving all other time points as observed, does not affect the model enough to alter the accuracy of the model on the test data. This information is unhelpful in identifying the aspects of the data that are important to the model for prediction. The application of the VEESA pipeline to this data, described in Section 3, produces non-zero PFI values, and the interpretation of the most important fPC (jfPC 1) provides a clear explanation as to the aspect of the data that is important to the model for prediction.

Since the predictor variables in the cross-sectional approach are highly correlated, we suspect that the non-zero PFI values are the result of accuracy being used as the metric. Consider the definition of accuracy. For a set of $i = 1, \dots, n$ observations, let y_i be the observed value and \hat{y}_i be the predicted value for observation i . Accuracy is computed as

$$Accuracy(y, \hat{y}) = \frac{1}{n} \sum_{i=1}^n I(\hat{y}_i = y_i).$$

With the simulated data, the predicted value is whether a function belongs to group 1 or 2. To compute the PFI for a time point, the observations across the simulated functions at

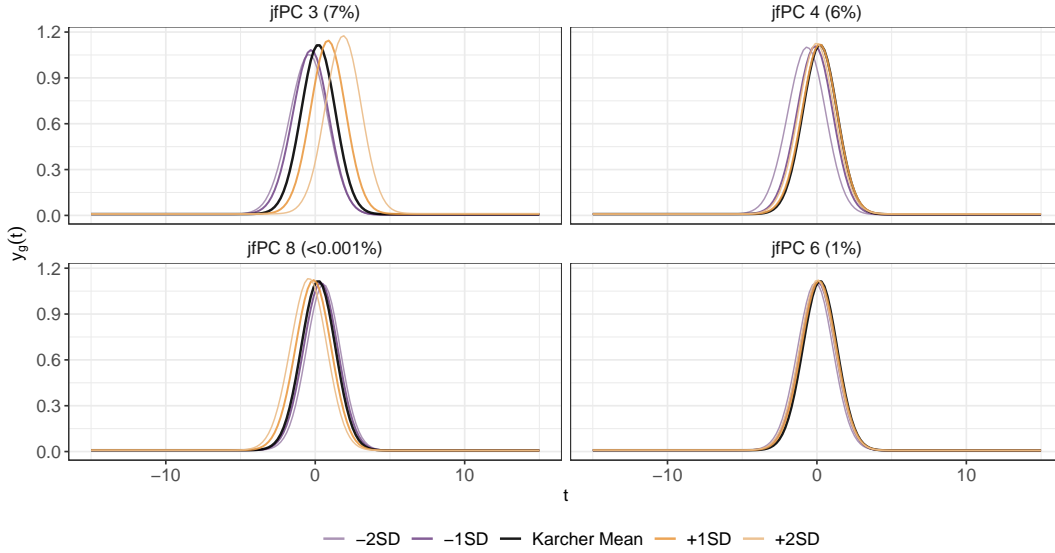


FIG 15. Principal direction plots of the VEESA pipeline jfPCs with log-loss based PFI values greater than 0.02 (excluding jfPCs 1 and 2 shown in Figures 2 and 4).

that time are permuted. With the remaining 149 time points being highly correlated with the permuted variable, enough information is likely provided to the model to produce the same prediction as to which group the function belongs to. However, a metric for a binary response variable based on the model probability that a function belongs to a group is more likely to be affected by the permutation of a single time point. One example of such a metric is log-loss. For $y \in \{0, 1\}$ and $p = P(y = 1)$ (estimated from a model), log-loss is defined as

$$LL(y, p) = y \log(p) + (1 - y) \log(1 - p).$$

To test this idea, we compute new PFI values using the log-loss metric for the random forest from the cross-sectional approach and the random forest in the VEESA pipeline. Both sets of PFI values are computed on the test data. Figures 14C and 14D depict the PFI values computed for the cross-sectional and VEESA pipeline approaches, respectively, using log-loss. As suspected, the log-loss metric produces non-zero values. However, note the difference in y-axis between the cross-sectional and VEESA pipeline PFI values. The cross-sectional PFI values are much smaller than the VEESA pipeline PFI values (i.e., the model predicted probability is much less affected when a variable is permuted). The cross-sectional PFI values suggest that the times between, approximately, $t = -2$ and $t = 2$ have little importance. The time points outside of this region have non-zero values. We may expect the times between -2 and 2 to have little importance since there is a lot of overlap between the two group during this time. We may also expect the times in the ranges of $t \in (-7, -2)$ and $t \in (2, 7)$ to be important since the groups are distinguished by their differing peaks associated with these intervals. However, the PFI values continue to be non-zero in the below -7 and above 7, where the the functions all have values of approximately zero. This result either suggests that the model is doing a poor job of using the information from the predictor variables, or more likely, these PFI values are biased due to the correlation between predictor variables.

The VEESA pipeline PFI values computed with accuracy (Figure 3) only found jfPCs 1 and 2 to be important for the test data. The log-loss metric identifies additional principal components as important, but jfPCs 1 and 2 remain the most important. Figures 2 and 4 showed that jfPC 1 and jfPC 2, respectively, capture variability in both the horizontal and vertical directions. Figure 15 includes the principal direction plots for the four other principal components with PFI (computed using log-loss) greater than 0.02. jfPC 3 focuses on

variability between functions with peaks similar to the mean around time 0 and functions with high peaks later than time 0. jfPCs 4 and 8 focus mostly on the horizontal variability between functions. jfPC 6 focuses on small amounts of horizontal variability. Although the VEESA pipeline results in a smaller (but similar) test data accuracy than the cross-sectional method, the feature importance results are more meaningful. The results are understandable in the data space of the problem and provide evidence for how the model is using the data for prediction.

To summarize, there are several concerns with the cross-sectional approach:

- The functional nature of the data is ignored. By treating each time point of samples as a predictor variable, the model is not aware of the relationship between samples within a function. By presenting the functions to the model in this form, information is lost. In some cases, the loss of information may lead to a loss in prediction performance.
- The horizontal variability in the functions is ignored. In the simulated data, the true functional means have different peak times, which leads to horizontal variability in the functions. The cross-sectional approach only uses the variability in the functions in the vertical direction to discriminate between the two classes. This effect is seen in the cross-sectional group means in Figure 14A. The shapes of the cross-sectional means do not accurately reflect the true functional means, because only the variability in the vertical direction is accounted when computing cross-sectional means in this manner.
- Correlation between the predictor variables can lead to bias in PFI. In practice, it may not be clear which PFI values are biased, so it becomes difficult to trust the results.

All three of these concerns are addressed by the VEESA pipeline through the use of efPCA.

7. H-CT Material Classification Additional Analyses. Additional details about the analysis of the H-CT material classification data are provided here. In particular, we present results comparing model accuracies from the cross-sectional approach, the three types of efPCA, and varying number of box-filter runs. We also include the PFI variability from the implementations of the VEESA pipeline included in the main text and the principal directions from the six most important jfPCs identified in the main text.

7.1. Smoothing Selection and Cross-Sectional Comparison. In order to select the number of box-filter iterations to use for the VEESA pipeline analysis of the H-CT material classification data, we consider a range of iterations and determine which leads to the best accuracy result on the test data. In the process, we implement the VEESA pipeline using jfPCA, vfPCA, and hfPCA, so we can compare their predictive performances. We also implement several variations of the cross-sectional approach for comparison. The details of the implementations for smoothing, the VEESA pipeline, and the cross-sectional approaches are described in the following paragraphs.

Smoothing A box-filter method is applied to smooth the H-CT data. The number of times the box-filter is run affects the smoothness of the functions (i.e., more runs lead to smoother functions). In order to determine the number times to run the box-filter, the box-filter is run 1, 5, 10, 15, 20, and 25 times.

VEESA Pipeline The VEESA pipeline is applied to all versions of the smoothed data using jfPCA, vfPCA, and hfPCA. A neural network is used as the model for each scenario. All models are trained with the default settings in *scikit-learn* (one layer with 100 neurons). The model accuracies are computed on the training and testing dataset.

Cross-Sectional Approach The cross-sectional approach is applied for comparison to the VEESA pipeline. Three variations in regards to smoothing are considered: applying the cross-sectional approach with (1) no smoothing, (2) after smoothing, and (3) after smoothing and

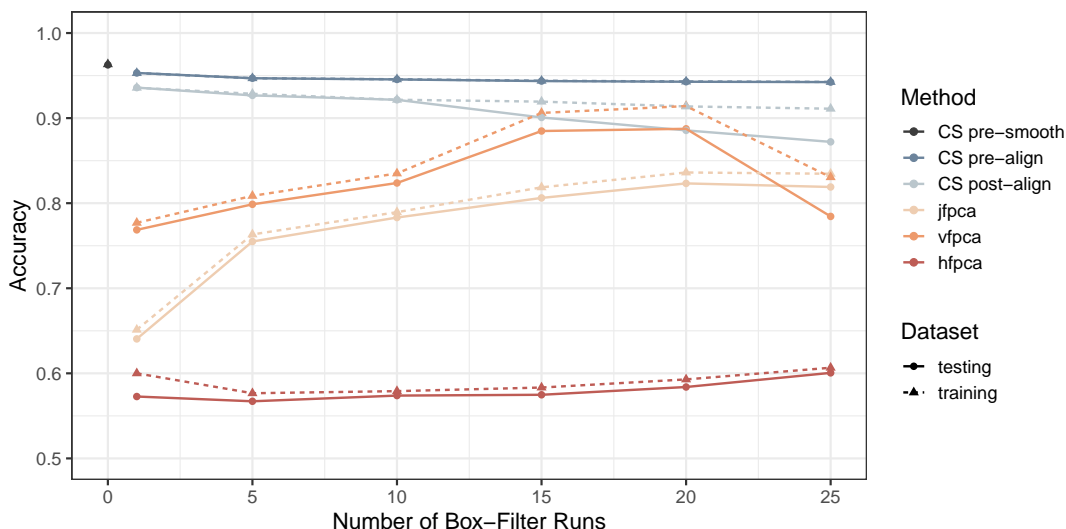


FIG 16. Model accuracies from neural networks applied using the VEESA pipeline and the cross-sectional approach.

ESA alignment. Again, neural networks are used as the model (trained in *scikit-learn* with default settings).

The model accuracies versus the number of box-filter runs are depicted in Figure 16 for all implementations. The colors represent the method used to process the data before training a neural network. The solid lines and circles indicate accuracy on the training data, and the dashed lines and triangles indicate accuracy on the testing data. The application of the cross-sectional method with no smoothing or alignment returns the highest accuracy. This is followed by the cross-sectional method with smoothing but no alignment with relatively consistent accuracy regardless of number of times the box-filter is run. The accuracies returned from the VEESA pipeline approaches are always lower on the testing data than training data. hfPCA results in the lowest accuracies followed by jfPCA, and vfPCA returns the highest accuracy for all box-filter iterations until 25. This is expected since it is understood that the vertical variability in the signatures contains the most information for material classification. The results from the VEESA pipeline using vfPCA and jfPCA when 15 runs of the box-filter are those displayed in the main text.

Even though the cross-sectional approaches lead to the largest accuracies (close to or above 0.9), the VEESA pipeline using vfPCA achieves accuracy values close to the cross-sectional accuracies when the box-filter is applied 15 and 20 times. In a high-consequence application, sacrificing some predictive performance for a method that returns more trustworthy explanations may be a necessity. However, no tuning of the neural network parameters was done, and work in this area could lead to increased predictive performance with the VEESA pipeline.

These results suggests two ideas for future work. It would be beneficial to compare the predictive performance of the VEESA pipeline to the cross-sectional approach in applications where horizontal variability contains predictive information to see if the explicit modeling of the horizontal variability affects performance. This analysis only considers training and testing sets. It would be beneficial to see how the cross-sectional and VEESA pipeline approach perform on a held out validation dataset.

7.2. PFI Variability and jfPCA Principal Directions. Figure 17 depicts the five feature importance replicates used to compute the PFI results included in the main text. The points are colored by the replicate with an alpha shading that provides transparency. However, all

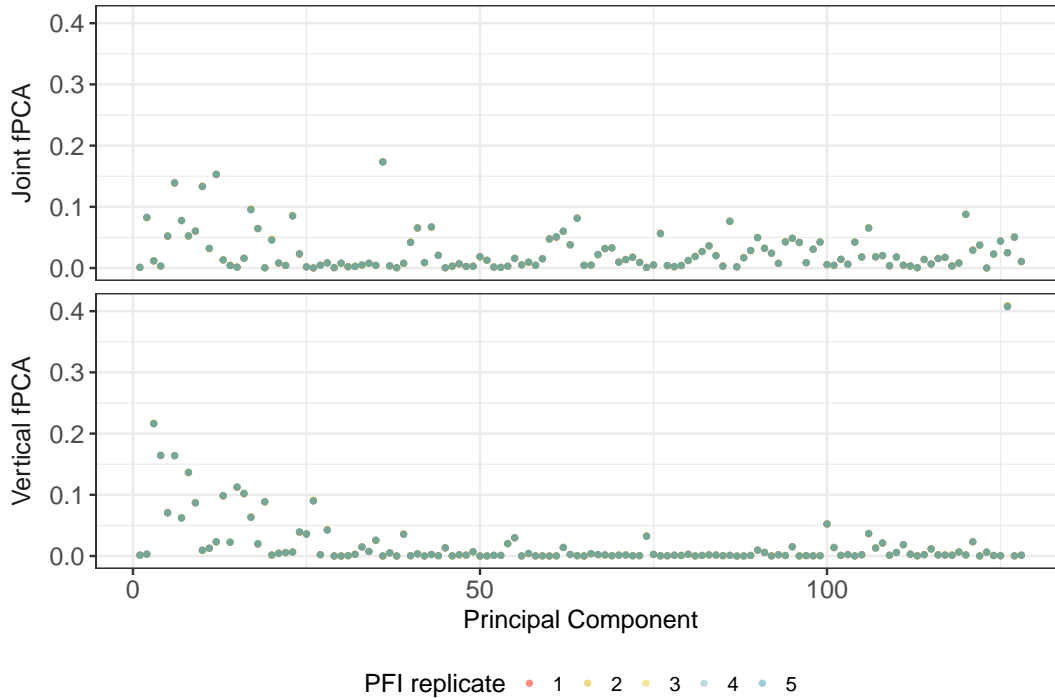


FIG 17. PFI replicate values for jfPCA (top) and vfPCA (bottom) associated with the H-CT material classification example.

points appear to be the same color, due to them overlapping. There is minimal amount of variability between the feature importance replicates.

Figure 18 depicts the principal direction plots of the four PCs with the highest PFI values from the jfPCA model. All four jfPCs capture aspects of both horizontal and vertical variability. The PC with the highest PFI (jfPC 36) focuses on vertical variability between functions with a horizontal shift from the mean at frequencies larger than 0.25. jfPC 36 also captures the change in variability around a frequency of 0.25.

8. Inkjet Printer Additional Analyses. We include some additional results from the inkjet printer analyses here: classification performance within each printer, principal directions for importance fPCs with magenta and yellow signatures, and an implementation of the VEESA pipeline for the worst performing scenarios with a subset of the principal components selected based on the feature importance in the main text.

8.1. Printer Classification Details. Figure 19 depicts confusion matrices for the three colors considered in the inkjet printer analysis in the main text. The true printer is listed on the x-axis, and the predicted printer is listed on the y-axis. The plots are generated using all test fold predictions for the best performing model for each color. These figures let us see which printers are challenging. For all colors, printers 7 and 8 often are predicted as the other printer. This is particularly true for magenta. Printers 7 and 8 have the same manufacturer and model, so it is understandable why these printers are more challenging. With cyan, printer 2 also stands out as being predicted incorrectly as printer 3. These two printers share the same manufacturer. With magenta, printer 11 is frequently mistaken for printer 10. Again, these printers share a manufacturer. With yellow printers 2 and 3 also are incorrectly predicted as the other printer. These results that the models tend to struggle to distinguish printers that are from the same manufacturer, which would be expected.

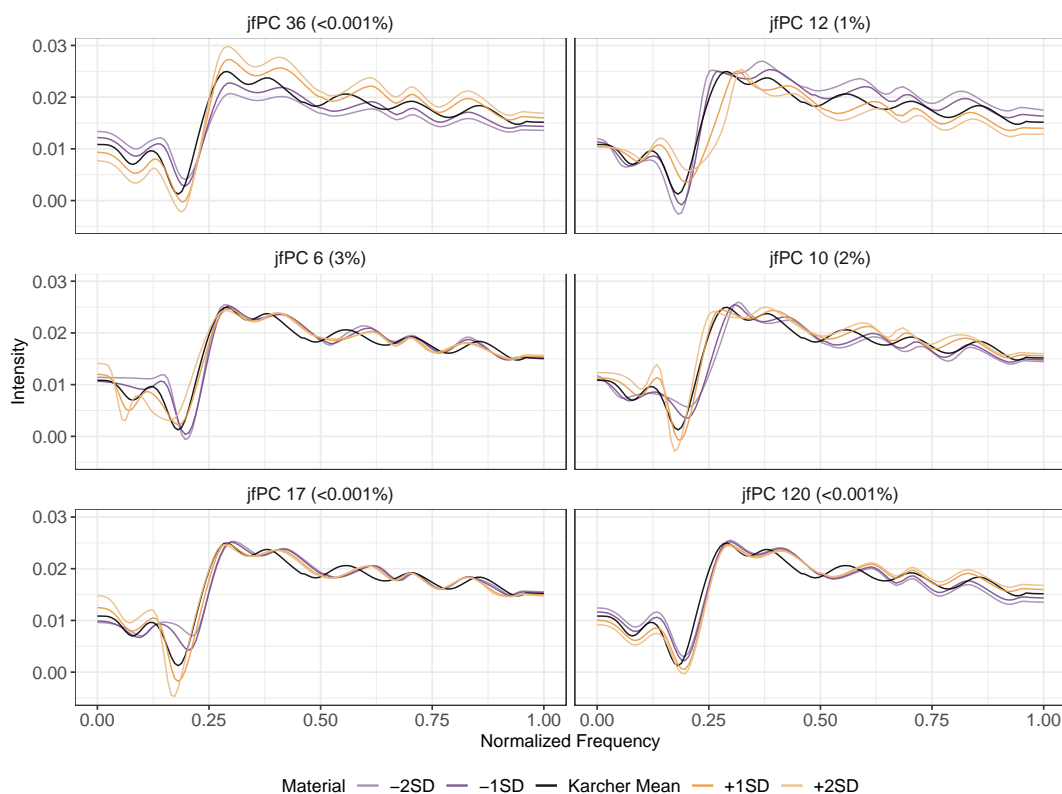


FIG 18. Principal directions from the six jfPCs with the highest PFI from the H-CT material classification example.

8.2. Principal Directions from Magenta and Yellow Signatures. Figure 20 shows the six most important PCs for the best (top) and worst (bottom) magenta models. The most important jfPCs for the best performing magenta model capture more horizontal variability than the jfPCs for cyan. For example, the most important jfPC for magenta (jfPC 1) captures variability between signatures that have peaks occurring immediately before and after 1250 cm^{-1} and signatures that are smoother besides for a slight increase around a wavenumber of 1200 cm^{-1} . This first PC appears to capture the variability in the magenta signatures between some printers that have dramatic peaks around 1250 cm^{-1} (e.g., printer 7) and other printers that gradually increase without such peaks and then decrease after 500 cm^{-1} (e.g., printer 4). The important fPCs for the worst magenta model capture similar aspects of the functional variability but with noisier functions.

Figure 21 shows the six most important PCs for the best (top) and worst (bottom) yellow models. The most important jfPCs for the yellow signature predictive model capture a combination of vertical variability across all wavenumbers and the horizontal variability around the peaks between wavenumbers of 1500 and 1000 cm^{-1} . The yellow signatures for all printers in Figure 9 have peaks in the range of wavenumbers of 1500 and 1000 cm^{-1} (unlike the magenta signatures), and there is more variability in the peaks in this range for the yellow signatures compared to the cyan signature peaks. Similar to cyan and magenta signatures, the amount that the signatures tends to increase as the wavenumber increases varies by printers, which is picked up by the important principal components. jfPC 2 for the yellow signatures is particularly interesting in that it appears to capture variability between signatures that have lots of peaks or noisy peaks in the range of 1500 and 1000 cm^{-1} (e.g., Printer 4) compared to signatures that do not have as many peaks (e.g., Printer 1). Again, the fPCs for the worst yellow model capture similar aspects of the variability but with noisier functions.

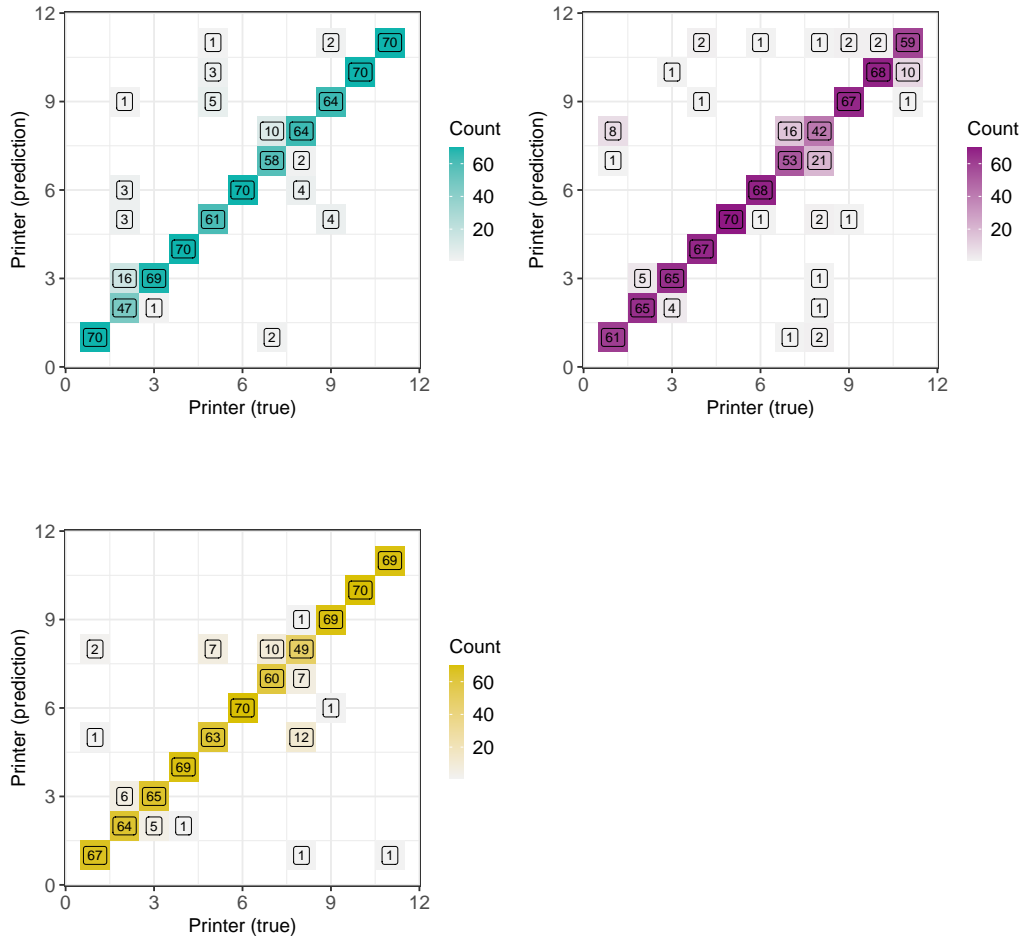


FIG 19. Confusion matrices for the inkjet printer random forests.

8.3. Improving Models Using PFI. As a last step in our analysis, we are interested in determining if we can make use of the information from the PFI results of the worst models to improve the predictive performance. We do this by implementing the cross validation procedure describe in the main text. However, for this implementation, we only consider random forests with 500 trees. We choose 500 trees, because it falls between the number of trees associated with the best performing models (i.e., 250 or 1000 trees). Additionally, we use PCs 1 to 25 and PCs 75 to 100 for all models based on the areas with important PCs as seen in Figure 11. We consider the same range of smoothing iterations (0, 5, 10, 15, 20, 25, 30, 35), and again, random forests are implemented separately by color. Figure 22 shows the average cross validation accuracies from this analysis.

In Figure 22, the plots of results are separated by color. The number of smoothing iterations is depicted on the x-axis, and the average accuracy is on the y-axis. The colored lines represent the accuracies from our original analysis (Figure 10), and the color of the lines indicates the number of PCs included in the model. The black line represents the average cross-validation accuracy from the updated models with the subset of fPCs selected based on the PFI results. For all smoothing iterations, the down selection of fPCs based on PFI led to a clear increase in test fold average accuracy. The accuracies are still lower than the best performing models, but this provides a case study where PFI provides useful information for improving model predictive performance.

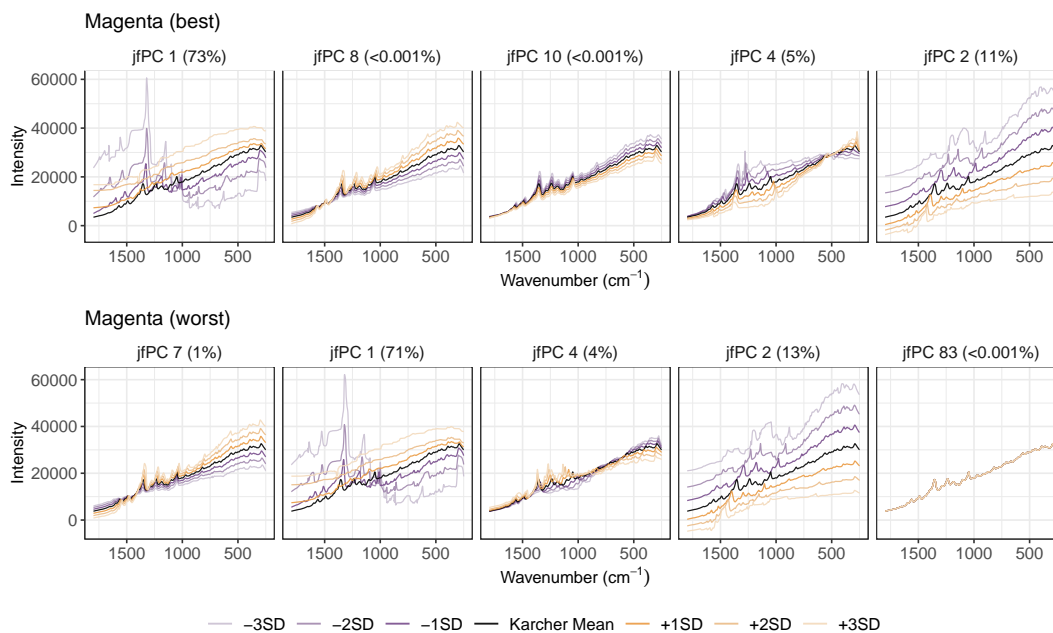


FIG 20. Principal directions from the best (top row) and worst (bottom row) models for predictions with magenta inkjet signatures. The jfPCs selected are those with the largest PFI values for their respective model. PCs are ordered from left to right based on highest to lowest feature importance.

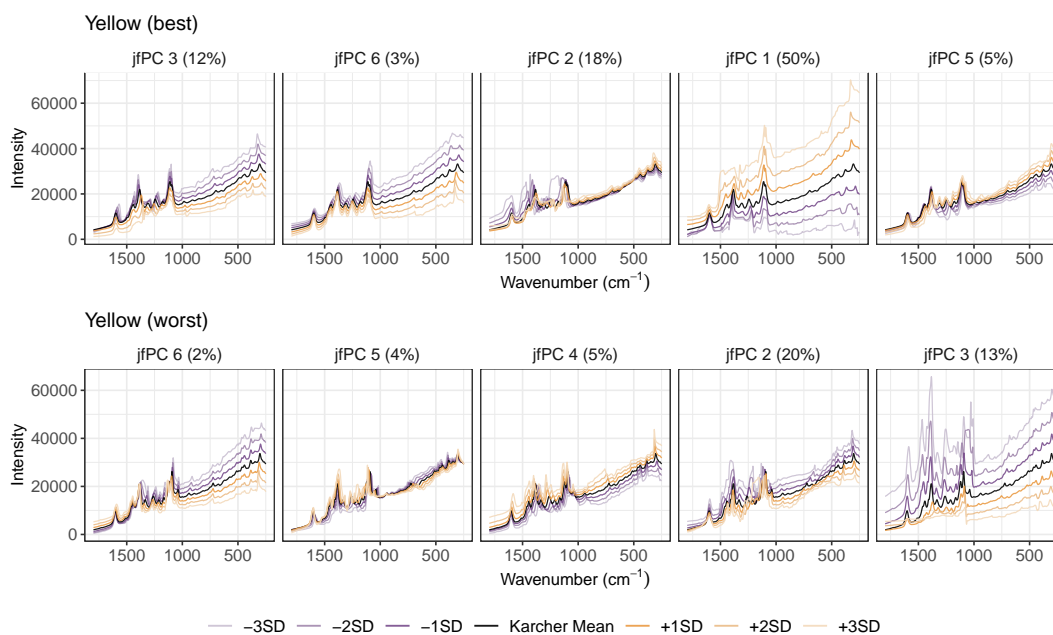


FIG 21. Principal directions from the best (top row) and worst (bottom row) models for predictions with yellow inkjet signatures. The jfPCs selected are those with the largest PFI values for their respective model. PCs are ordered from left to right based on highest to lowest feature importance.

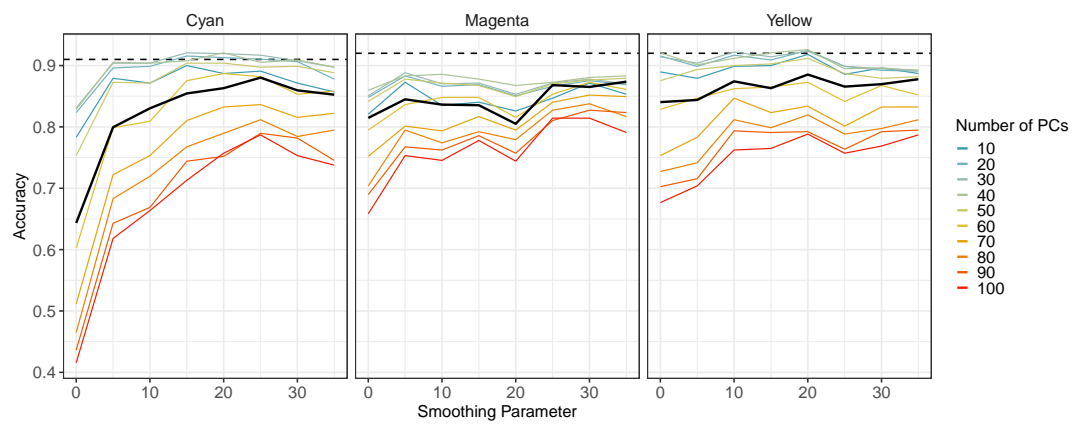


FIG 22. Cross validation average accuracies. Black lines represent CV accuracies from models with PC selected via PFI.